GROWTH, AND CHARACTERIZATION OF $Mn_{2-x}CoGe$, $Mn_{2-x}RhGe$ AND $Mn_{2-x}CoGe$ THIN FILMS

by

David Kalliecharan

Submitted in partial fulfillment of the requirements
for the degree of Master of Science

at

Dalhousie University
Halifax, Nova Scotia
December 2018

In memory of my parents, and godparents: Rajdeo and Debra Kalliecharan; John and Maria Maas.

This work is dedicated to Peter Kalliecharan—my brother—including his wife and son, Michaela and Jasper.

Table of Contents

List of Tables . . . . . **v**

List of Figures . . . . . **vi**

Abstract . . . . . **xii**

List of Abbreviations and Symbols Used . . . . . **xiii**

Acknowledgements . . . . . **xv**

Chapter 1 Introduction **1**

1.1 Heusler compounds, and structures 3
1.1.1 Half-Heuslers XYZ 4
1.1.2 Full-Heuslers X_2YZ 4

1.2 Hexagonal Ni_2In-type structure 7
1.2.1 Magnetic bubble: biskyrmion 7
1.2.2 Magnetic Refrigeration: Permament magnets 8

1.3 Hexagonal $P\bar{6}2m$ and orthorhombic $Ima2$ structures 9

Chapter 2 Film Deposition **11**

2.1 Sputtering deposition 11

2.2 Substrate preparation 13
2.2.1 SiO_2 diffusion barrier 14

2.3 Rapid thermal annealing RTA 14

Chapter 3 Methods, and Techniques **15**

3.1 X-ray diffraction (XRD) 15
3.1.1 Grazing angle XRD: Thin-film characterization 17

3.2 Magnetic characterization 20
3.2.1 Magnetic hysteresis 20
3.2.2 Remanent magnetization measurement 22

Chapter 4 $Mn_\alpha CoGe$ alloys **24**

4.1 $Mn_{2.0}CoGe$ 31

4.2 Magnetic characterization 33

Chapter 5 $Mn_\alpha RhGe$ alloys 40

5.1 Magnetic characterization 45
5.1.1 Ni_2In-type structures 45
5.1.2 Fe_2P-type, and TiFeSi-type structures 48

Chapter 6 $Mn_\alpha IrGe$ alloys 51

6.0.1 Future Work 54

Chapter 7 Conclusion 56

Bibliography 60

Appendix A Magnetron calibration curves 66

Appendix B Stoichiometry uncertainty 68

List of Tables

1.1 Tetragonal and cubic lattice parameters for DFT predicted germanium Heusler alloys. The tetragonal (*tet*) phase has a lower energy than the cubic (*cub*) phase in each case. 3

3.1 Mass attenuation coefficient values from NIST at 8 keV. 19

4.1 Thermal expansion coefficients 28

4.2 $Mn_{\alpha}CoGe$ parameters extracted from XRD. Thin-film lattice parameters varied by ± 0.005 Å. 32

4.3 $P6_3/mmc$ Magnetic properties of $Mn_{\alpha}CoGe$ 35

5.1 $Mn_{\alpha}RhGe$ parameters extracted from XRD, and comparisons. . 44

5.2 Magnetocrystalline anisotropy comparison. 48

5.3 $Mn_{\alpha}RhGe$ magnetic characteristics and comparisons. 50

6.1 $Mn_{2.0}IrGe$ Ni_2In-type parameters 51

6.2 Summary of Ni_2In-type lattice parameters and magnetic characteristics. 54

List of Figures

1.1 Racetrack memory illustrating magnetic domain walls that are driven along a wire by electrical currents. A read head can determine the polarity of the domain as it moves by, and a write head can inject a domain. Figure adapted from [1]. . . . 1

1.2 (a) Block skyrmion, (b) Néel skyrmion and (c) antiskyrmion. The colour of the spin represents the magnitude of the $\hat{z}$ component of the spin. 2

1.3 (a) A rock salt structure with 4a (blue) and 4b (red) Wyckoff positions, and (b) a zinc blende structure with 4a (blue) and 4c (black) Wyckoff positions. Merging the two substructures yields (c), the half-Heusler structure depicting the 4a (blue), 4b (red), and 4c (black). 5

1.4 The regular full-Heusler structure (a) depicting Wyckoff positions at 8c (black), 4a (blue), and 4b (red). The inverse full-Heusler structure (b) depicting the Wyckoff positions 4a, and 4c (black and green), 4d (blue), and 4b (red). The tetragonal inverse full-Heusler structure (c) can be visualized from the dotted lines in (b), but is elongated along the c direction. The view along the (111) direction is below the isometric view of the Heusler structures. 6

1.5 Some Co_2 based Heusler compounds showing the magnetic moment is proportional to the valence electrons, and is in good agreement with the Slater-Pauling curve (stylized from [2]). . . 7

1.6 Ni_2In-type structure with Wyckoff positions 2a (black), 2c (red), and 2d (blue). 8

1.7 Fe_2P-type structure with atoms X (black on 3g sites), Y (red on 3f sites) and Z (blue on 1b and 2c sites). 9

1.8 TiFeSi-type (I$ma2$) structure with atoms X (black), Y (red) and Z (blue). 10

2.1 Outline of DC magnetron sputtering within an Ar gas environment. Desired target material atoms (small green circles) are ejected from Ar ions colliding with the target; the ejected atoms deposit onto the substrate (magenta). 12

2.2 Corona Vacuum Coater V3T system configuration used for depositing Mn, {Co, Rh, Ir}, and Ge compounds. The samples (squares) are situated so they pass over the middle of the targets as the circular table is rotated. 13

3.1 Bragg's law showing constructive interference by d spaced planes (a), and an Ewald's sphere demonstrating the conditions for constructive interference, which occurs when the difference between the incident wavevector k_i and outgoing wavevector k_f is equal to a reciprocal lattice vector, G. 15

3.2 XRD setup depicting X-ray source, detector, sample stage, and slits for $\theta - 2\theta$ scans. 17

3.3 Glancing angle XRD configuration. Source is fixed (a), while the detector swept through a 2θ scan. The red, and blue arrows depict the normals to the planes that the detector is sensitive to for the two detector positions shown. 18

3.4 Varying incident angle θ_i in GAXRD measurements gives insight into the preferred orientation of a textured $Mn_{2.0}RhGe$ film. The shaded regions highlight the (002) and (110) peaks whose intensity varies greatly with grazing angle relative to the other crystallographic orientations. 19

3.5 PPMS detector coil configuration. Sample oscillates between the two sets of coils within a constant applied field $\mu_0 H_{\text{ext}}$ to and measures the derivative of the magnetization via current loops. The samples are stacked in sets of 2 or 3 with their normal, $\hat{n}$, perpendicular to the oscillation to measure the in-plane magnetization. 20

3.6 Magnetic hysteresis curves depicting saturation magnetization, remanent magnetization, and coercive field. 21

3.7 (a) An ensemble of magnetic single domain particles, where the spins align along the particle's easy axis. (b) An external field applied at an angle θ_0 with respect to the easy axis; this causes the moment to kant towards H_{ext} at angle θ with respect to the field. 22

3.8 (a) A set of single domain hysteresis loops from the Stoner-Wohlfarth model as a function of θ_0. The average of these loops yield the $M - H$ curve (b) for a random distribution of uniaxial single domain particles. 22

3.9 A typical $M_R - T$ curve, with the estimate of the Curie temperature T_C highlighted by the red dashed line. 23

4.1 XRD pattern of $Mn_{2.0}CoGe$ grown on the native oxide on a Si(001) wafer and annealed at 700 °C, showing diffusion into Si(001) substrate. The sample has peaks identified as MnSi, $MnSi_{1.7}$, and Ge. 25

4.2 XRD patterns for $Mn_{1.4}CoGe$: $\theta - 2\theta$ (black), and GAXRD (red); The substrate 100 peak can still be seen at 69.9 ° in the $\theta - 2\theta$ XRD pattern even though the sample angle is offset by 2°. The inset shows peak location differences between GAXRD and XRD. 26

4.3 XRD and GAXRD patterns for powder Si. The inset shows peak location differences between GAXRD and XRD. 27

4.4 XRD patterns for $Mn_{1.5}RhGe$: $\theta - 2\theta$ (black), and GAXRD (red); show consistent peak positions, but still exhibit differences in intensity. The substrate 100 peak can still be seen at 69.9 ° in the $\theta - 2\theta$ XRD pattern. 28

4.5 (a) Geometry of a crystallite whose normal is offset from the substrate normal, where θ_i is the incident grazing angle and 2θ is the angle of the detector. (b) Unstrained planes, spaced by d, on the left (red) whose normal is offset by ϕ from the normal of the substrate. Strained planes, spaced by d', on the right (blue) whose normal is offset by ϕ', with strain transformation applied to the Cartesian grid. The function $u(x)$ is defined as the strain tensor, that deforms the planes. 29

4.6 The ratio of d-spacings, $d'(\phi)/d'(0)$ for $Mn_{1.4}CoGe$. Where $d'(\phi)$ is the plane spacing from GAXRD, and $d'(0)$ is the spacing obtained from XRD. 31

4.7 GAXRD refinements for $Mn_{1.0}CoGe$, $Mn_{1.4}CoGe$, and $Mn_{2.0}CoGe$ thin-films that were annealed for 2 minutes at 400 °C for (a) and (b), while (c) became stable at 500 °C for 2 minutes. These patterns were measured for a dwell time of 17 s. Crystal phase identified as $P6_3/mmc$ Ni_2In-type structure, with peak locations shown in (c). 34

4.8 Magnetic hysteresis curves for $Mn_{\alpha}CoGe$ ternary compounds at 5 K. Magnetization per volume shows M_{sat} for $Mn_{1.0}CoGe$, $Mn_{1.4}CoGe$ and $Mn_{2.0}CoGe$ to be 377 kA/m 422 kA/m, and 345 kA/m respectively. The coercive fields for $Mn_{1.0}CoGe$, $Mn_{1.4}CoGe$ and $Mn_{2.0}CoGe$ are $\mu_0 H_C$=0.0272 T, $\mu_0 H_C$=0.079 T and $\mu_0 H_C$=0.089 T respectively. 35

4.9 Remanent magnetization M_R versus temperature. $Mn_{2.0}CoGe$ (blue) has an expected remanent magnetization curve with T_C at 259 K, $Mn_{1.0}CoGe$ (black) M_R curve shows evidence of ferrimagnetic-like behaviour, with a T_C of 259 K, and $Mn_{1.4}CoGe$ (red) showing evidence of a secondary phase. 36

4.10 A recreated representation of a N-type ferrimagnetic $M_R - T$ curve from Chikazumi et al. [3], showing the compensation point T_{cmp}, where the two magnetic sublattices (red, and blue) sum to zero, and the Curie temperature T_C of the system. The dashed black lines is representative of the situation such that the applied field is low enough where the magnetization doesn't reverse above T_{cmp}. 37

4.11 The removal of soft a secondary magnetic phase by annealing $Mn_{2.0}CoGe$ to 500 °C for 2 minutes. This is compared to $Mn_{2.0}CoGe$ and $Mn_{1.4}CoGe$ annealed at 400 °C for 2 minutes. 38

4.12 Hypothesis of two ferromagnetic domains that are antiferromagnetically coupled, where the moments are not equal in magnitude. The $Mn_{2.0}CoGe$ M_R (blue) curve is used as an estimate of the M_R of one magnetic sublattice (magenta) of the $Mn_{1.0}CoGe$ M_R curve (black), the difference yields the hypothetical M_R-T curve of the second sublattice (green). 39

5.1 GAXRD diffraction pattern for $Mn_{1.0}RhGe$ annealed at 700 °C for 12 minutes, with two distinct phases: MnRhGe P$\bar{6}$2m Fe_2P-type structure, and RhGe Pnma structure. 41

5.2 GAXRD patterns for $Mn_{1.0}RhGe$ (a), $Mn_{1.5}RhGe$ (b), and $Mn_{2.0}RhGe$ (c) found at annealing temperature of 700 °C. The P$\bar{6}$2m phase is found on $Mn_{1.0}RhGe$ and $Mn_{1.5}RhGe$ after annealing at 12 minutes and 47 minutes respectively. The Ima2 TiFeSi-type structure is found on $Mn_{2.0}RhGe$ after 17 minutes of annealing. The crystal peaks for P$\bar{6}$2m (blue), and Ima2 (magenta) are located below the residuals of the relevant fits. 42

5.3 GAXRD of the $Mn_{\alpha}RhGe$ showing the difference between the Ima2 and P$\bar{6}$2m structures. 43

5.4 Discrepancy of 002, 102 and $2\bar{1}0$ peaks for the $Mn_{2.0}RhGe$ Ni_2In-type structure in GAXRD, and XRD. The preferred orientations are possibly due to the surface energy differences from the $Mn_\alpha CoGe$ because Rh has a higher annealing temperature. 43

5.5 GAXRD patterns of $Mn_{1.5}RhGe$, and $Mn_{2.0}RhGe$ show $P6_3/mmc$ Ni_2In-type structures. Annealing of the Ni_2In-type structures found (a) $Mn_{1.5}RhGe$ at 700 °C, and (b) $Mn_{2.0}RhGe$ at 500 °C. 44

5.6 $Mn_{2.0}RhSn$ annealed at 700 °C for 2 minutes with preliminary results for the tetragonal $I\bar{4}m2$ structure (red). It is likely that material has a secondary phase for the unaccounted peaks. . . 45

5.7 Scanning electron microscopy images showing evidence of grains on the order of 70 nm, found in $Mn_{2.0}RhGe$ of Ni_2In-type. . . 45

5.8 The magnetic hysteresis curves for $Mn_{1.5}RhGe$ (red) and $Mn_{2.0}RhGe$ (dotted blue) $P6_3/mmc$ Ni_2In-type structures, with M_{sat} values at 341.9 kA/m and 389.2 kA/m respectively. The solid blue curve shows $Mn_{2.0}RhGe$ after subtracting the soft magnetic phase. 46

5.9 Remanent magnetization curves showing the T_C for $Mn_{1.5}RhGe$ (red), and $Mn_{2.0}RhGe$ (blue) Ni_2In-type structures. Curie Temperatures of $Mn_{1.5}RhGe$, and $Mn_{2.0}RhGe$ are estimated to be 307 K. 47

5.10 The Stoner-Wohlfarth model (red) overlayed on top of the $Mn_{2.0}RhGe$ magnetic hysteresis curve. 48

5.11 Magnetic hysteresis curves for $P\bar{6}2m$ phases $Mn_{1.0}RhGe$ (a) and $Mn_{1.5}RhGe$ (b), with the $Ima2$ phase $Mn_{2.0}RhGe$ (c). Hard magnetic impurity present on $Mn_{2.0}RhGe$ (c), the opposite of the $Mn_{2.0}RhGe$ Ni_2In-type phase (Fig 5.8). 49

5.12 Remanent magnetization for the $P\bar{6}2m$, and $Ima2$ phases of the Mn, Rh, and Ge ternary alloys show that the Curie temperature is well above 350 K. Magnetic impurity phases can be seen in the Curie temperature curves, but this is due to annealing temperature, and duration choices. 49

6.1 $Mn_{2.0}IrGeGAXRD$ pattern displays the $P6_3/mmc$ Ni_2In-type structure, similar to $Mn_\alpha\{Co, Rh\}Ge$. The inset shows the $\theta - 2\theta$ XRD, with the 002 peak intensity dominating the diffraction pattern; the fit is shown in red, the residuals in green. 52

6.2 The 5 K magnetic hysteresis curve (dotted blue) for $Mn_{2.0}IrGe$ with a $\mu_0 H_C = 4.84$ T, and a $M_{\text{sat}} = 103.8$ kA/m. The 300 K magnetic hysteresis is shown to highlight a softer magnetic secondary phase with the $\mu_0 H_C = 0.011$ T, and M_{sat} 19 kA/m. 53

6.3 The $Mn_{2.0}IrGe$ T_C curve has similar characteristics to other $P6_3/mmc$ Ni_2In-type structures compared to the Co, and Rh variants. The Ni_2In-type $Mn_{2.0}IrGe$ has the lowest T_C of 224 K of all compounds presented in this research. 53

6.4 Diffractions patterns of $Mn_\alpha IrGe$ at 700 °C: (a) The $Mn_{1.0}IrGe$ annealed for 2 mintues, (b) $Mn_{1.5}IrGe$ annealed 22 minutes and (c) $Mn_{2.0}IrGe$ annealed for 2 minutes. Potential cubic and tetragonal phases for (a) and (b) can be seen in (d). 54

7.1 M_{sat} comparison of Ni_2In-type $Mn_\alpha\{Co, Rh, Ir\}Ge$ structures. 56

7.2 A comparison of the $M - H$ loops for $Mn_{2.0}CoGe$, $Mn_{2.0}RhGe$ and $Mn_{2.0}IrGe$ to emphasize how the hysteresis changes with increasing atomic number. 57

7.3 $mu_0 H_C$ comparison of Ni_2In-type $Mn_\alpha\{Co, Rh, Ir\}Ge$ structures. 57

A.1 Calibration for Mn and Ge targets in an 2 mTorr Ar environment 66

A.2 Calibrations for Co, Rh and Ir targets in an 2 mTorr Ar environment 67

B.1 Al sputter depositon profile that compares the presence of magnetic steel screws to brass screws on the sputter substrate table. 68

B.2 Sputter substrate table layout for measuring the sputter deposition profile around the table at a radius 13.3 cm from the table centre. The dashed grey lines represent the placement of the big screws in Fig B.2. 69

Abstract

Skyrmions are the smallest possible thermodynamically stable magnetic state, and are therefore promising objects for information storage. New tetragonal structures within the vast Heusler family of compounds are predicted by density functional theory (DFT) to be skyrmion hosting candidates. This work explores the crystal structure and magnetic properties of sputtered thin-films of $Mn_{1\leq\alpha\leq2}${Co,Rh,Ir}Ge ternary compounds. These ternary compounds predominantly formed two hexagonal ($P6_3/mmc$ and $P\bar{6}2m$) structures. Mn_αCoGe films formed a Ni_2In-type ($P6_3/mmc$) structure which had not been previously observed. The saturation magnetization, M_{sat}, for Co and Rh variants are 20%–30% lower than MnCoGe bulk of M_{sat}=2.78 μ_B per formula unit (f.u.). However, the M_{sat} for $Mn_{2.0}$IrGe was significantly lower. The Curie temperatures, T_C, for Co variants were comparable to bulk MnCoGe at T_C=260 K. The larger spin-orbit interaction in Ir and Rh compounds resulted in an increase in coercive field: In the case of $Mn_{2.0}$IrGe of $\mu_0 H_C$=4.84 T at a temperature of 5 K. For MnRhGe and $Mn_{1.5}$RhGe films, a hexagonal Fe_2P-type ($P\bar{6}2m$) structure was identified as the stable phase. However, the Fe_2P-type structures have a much smaller magnetocrystalline anisotropy, with a coercive field that is up to 55 times smaller than found in the Ni_2In-type structure. None of the thin-films studied in this dissertation demonstrate the DFT calculated Heusler structures. This indicates that the hexagonal phases must be considered when predicting the stable structure of the intermetallic germanides.

List of Abbreviations and Symbols Used

2θ	X-ray diffractometer Detector angle.
A	Exchange constant.
H_C	Coercive field.
H_{ext}	External applied field.
I_0	Incident intensity.
I	Intensity.
K_u	Magnetocrystalline anisotropy.
L	Attenuation length.
M_R	Remanent magnetization.
M_{sat}	Saturation magnetization.
$S(\vec{G})$	Structure factor.
T_C	Curie Temperature.
$V_n(\vec{G})$	Scattering potential of the n^{th} atom.
λ_{fp}	Mean free path.
λ	Wavelength.
μ/ρ	Mass attenuation coefficient.
μ	Attenuation coefficient.
ρ	density.
θ_i	Incident angle.
$\vec{G}$	Reciprocal lattice vector.
$\vec{r_n}$	Atomic position vector.
$f_n(\vec{G})$	Form factor.
f_p	Footprint.
k_f	Outgoing wavevector.
k_i	Incident wavevector.
q	Scattering vector.
w_i	Atomic weight.
z_L	X-ray penetration depth.

d	Plane spacing.
BOX	Burned in oxide.
DFT	Density functional theory.
DMI	Dzyaloshinskii-Moyira interactions.
f.u.	Formula unit.
fcc	Face centred cubic.
GAXRD	Grazing angle X-ray diffraction.
MCE	Magnetocaloric Effect.
PPMS	Physical properties measurement system.
RM	Racetrack memory.
RTA	Rapid thermal annealer.
SOI	Silicon on insulator.
XRD	X-ray diffraction.

Acknowledgements

One conversation I had with a former employer before leaving to continue my studies at Dalhousie was, "Surround yourself with people who want you to see you succeed and you will get there". Over the course of my time spent at Dalhousie University, I met a breadth of people who have helped me over the course of undergraduate, and graduate studies. My experiences at the Department of Physics have shown me that the friends and colleagues in this community are motivated to help anyone succeed.

My supervisor—Theodore Monchesky—has been instrumental to me as an educator, supervisor, and friend. In my time at Dalhousie, he has provided advice on physics, a future career and life at almost any hour of the day (or those late nights). Ted's dedication to education and to all those around him inspired me to persue a career in Physics, and in turn, I hope to inspire those around me to have the resources to move forward along their own paths. I cannot properly articulate the gratitude I have towards having the opportunity to study under Ted.

Over the course of this research, my current lab group members Jason McCoombs and Brett MacNeil; former lab mate Simon Meynell have been invaluable as friends and colleagues over my time in graduate studies. They created a jovial lab environment that is always welcoming, and I always look forward to coming to work. This research would not have seen the light of day, if it was not for the help and time that these individuals have clocked in.

The staff of the physics department feels like an extended family to me. Our resident technologist, Andrew George, has helped me over the course of my time at Dalhousie with many projects—to many to count—providing advice on techniques that I would have never of thought of. The machinists, Kevin Borgel and John Noddin always available to help with cleverly designing equipment. The office staff: Tanya Timmins, Jennifer Curie, Heather-Anne Jennex and Valerie O'Neill always making sure I take time for myself, and share a laugh. Michel Johnson, for assistance with magnetic measurements and troubleshooting.

I would like to thank my committee members, Jeff Dahn and Laurent Kreplak.

Jeff, thank you for providing the equipment and resources to conduct this research. Without his donation, this research would not have been possible. Laurent, for taking the time out of his schedule to agree to be a reader. Both of you have been an inspiration to me over the course of my undergraduet studies in the way you approach physics.

All of my professors have helped me along the way, but I would like to acknowledge a few of them. Daniel Labrie, for providing the opportunity in undergrad to be a research assistant. Andrew Rutenberg, thank you for making theoretical physics approachable and giving entertaining lectures.

Lastly, the friends I have made over the course of my graduate studies: Marc Cormier, Allan Hupman, John Lincoln, Emma Shouldice, Carmen Lee, Tolson Winters, Beth Castle, Kaja Rotermund, Kevin LaCaille, Alyson Spitzig, Tim Miller, Charlotte Clegg, and Ajan Ramachandran. Your friendship can never be replaced.

The people mentioned here have been instrumental as friends, colleagues and I regard them as an extended family. You have provided a memorable experience for my time at Dalhousie, that I am truly grateful for, thank you.

Chapter 1

Introduction

Magnetic storage has been the primary storage medium for the digital age. Starting initially as magnetic tape storage and advancing towards magnetic platter hard disk drives (HDD) as the backbone of modern information. Consumer and corporation demands have consistently driven the market towards higher density storage, and lower power requirements, with new materials driving research interests into new magnetic storage technology to meet the demand.

One emergent technology—racetrack memory (RM)—uses electrical currents to move magnetic domains along a wire, as illustrated in Figure 1.1. Information is encoded in the direction of the magnetization of the domains. The information can be read, or written with magnetic tunnel junctions (MTJ) [4].

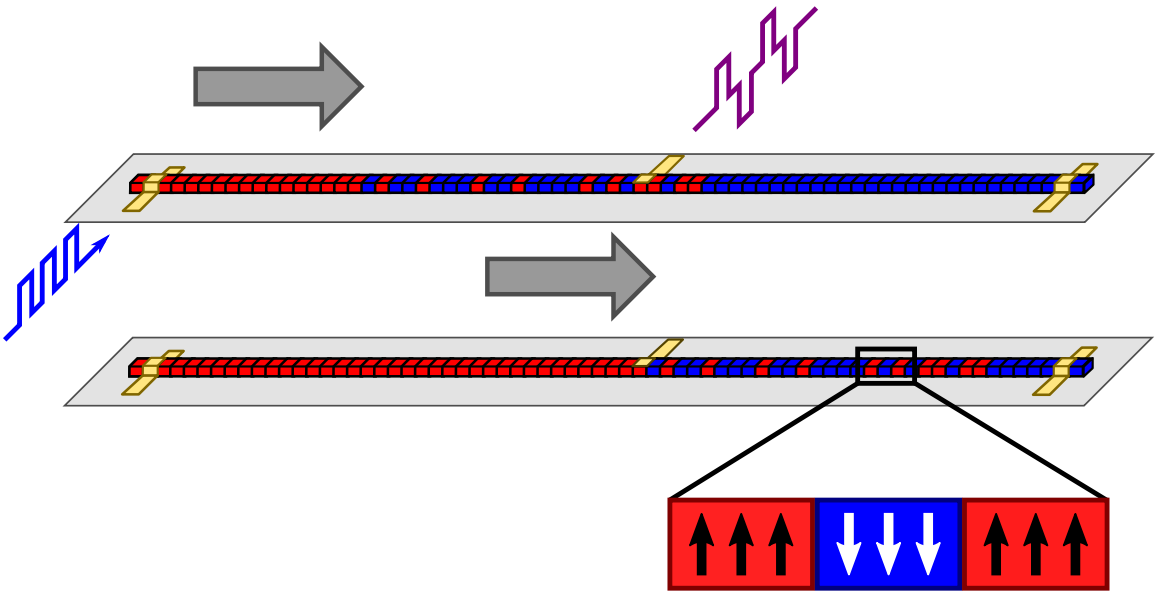

Figure 1.1: Racetrack memory illustrating magnetic domain walls that are driven along a wire by electrical currents. A read head can determine the polarity of the domain as it moves by, and a write head can inject a domain. Figure adapted from [1].

One can augment RM technology by chiral magnetic materials. A magnetic chiral interaction known as the Dzyaloshinskii-Moriya interactions (DMI) is present if the lattice of material lacks crystal inversion symmetry [5, 6]. Chiral magnetic interactions can lead to the information of 2 dimensional magnetic textures known as skyrmions. These cylindrical magnetic objects are the smallest possible thermodynamically stable state in a magnetic material [7]. Skyrmions are typically tens of nanometers in diameter, and therefore capable of higher density storage capacity than magnetic domains [8]. Figure 1.2 shows 3 kinds of skyrmions. The winding of the spins in the skyrmions is determined by the crystal structure: for example structures with T point group symmetry can host Bloch skyrmions (Fig 1.2a), and crystal structures with C_{2v} symmetry can host Néel skyrmions (Fig 1.2b). Structures with D_{2d} symmetry give rise to antiskyrmions (Fig 1.2c).

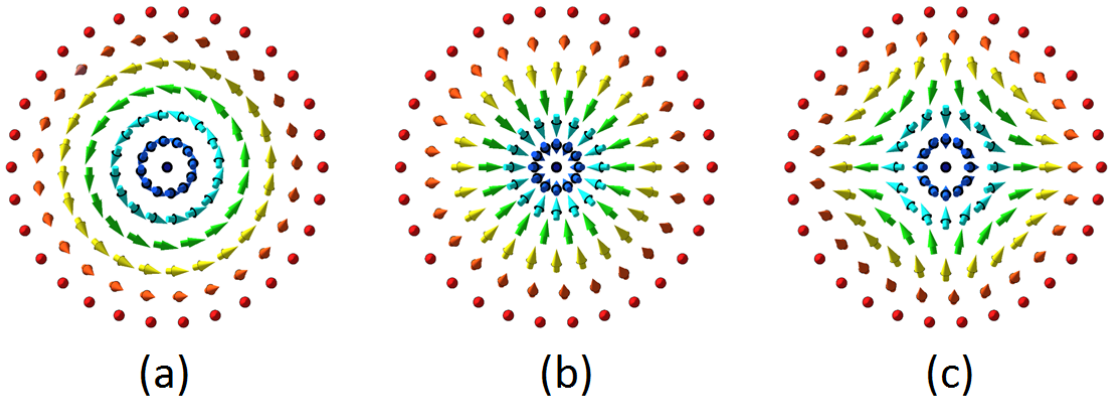

Figure 1.2: (a) Block skyrmion, (b) Néel skyrmion and (c) antiskyrmion. The colour of the spin represents the magnitude of the $\hat{z}$ component of the spin.

The presence of skyrmions in a material requires that the operating temperature is below the Curie temperature (T_C) [6, 9, 10]. MnSi is a well studied material that was a research testbed for skyrmions, but is not feasible for RM technology since the T_C=29 K is far too low [11, 12]. There is a need to find suitable materials to host stable skyrmions well above room temperature. A new family of materials that are of interest for skyrmions are the Heusler alloys, with over 2000 cubic or tetragonal possible compounds with 1:1:1 or 2:1:1 stoichiometry. Density functional theory (DFT) of a subset of 284 alloys were investigated to determine candidates that would have broken inversion symmetry [13]. Ferromagnetic Heusler compounds that

Table 1.1: Tetragonal and cubic lattice parameters for DFT predicted germanium Heusler alloys. The tetragonal (*tet*) phase has a lower energy than the cubic (*cub*) phase in each case.

Alloy	a_{tet} (Å)	c_{tet} (Å)	a_{cub} (Å)
Mn3Ge	3.73	7.087	4.06
Mn2FeGe	3.62	7.457	4.05
Mn2CoGe	3.74	6.882	4.06
Mn2NiGe	3.73	7.087	4.13
Mn2CuGe	3.77	7.163	4.15
Mn2RuGe	3.81	7.315	4.17
Mn2RhGe	3.85	7.238	4.18
Mn2PdGe	3.91	7.429	4.33
Mn2OsGe	3.81	7.391	4.18
Mn2IrGe	3.83	7.354	4.19

a have non-centrosymmetric crystal structure are potential candidates for hosting skyrmions [2, 14, 15, 16]. There are currently only two examples of a Heusler which have been shown experimentally to host skyrmions: $Mn_{1.4}RhSn$ and $Mn_{1.4}Pt_{1-x}Pd_xSn$ (Pd doped) have D_{2d} symmetry and form antiskyrmions at room temperature [17]. DFT, however, predicts a large number of Heusler alloys with the same D_{2d} symmetry. This dissertation was motivated by trying to find suitable alloys to host skyrmions from the germanide Heusler compounds, as these are predicted to be lattice matched to Si(001) (see Table 1.1). The scope will be further limited to $Mn_\alpha XGe$ alloys where X is a Group IX element, {Co, Rh, Ir}. However, this dissertation shows that the sputtered films do not have the structure predicted for all of these alloys Instead, the centrosymmetric Ni_2In-type structure ($P6_3/mmc$) forms at low annealing temperatures. At high annealing temperature a transition to other structures is observed but the desired $I\bar{4}2m$ structure was not found.

1.1 Heusler compounds, and structures

The Heusler compound Cu_2MnAl was first discovered by Fritz Heusler in 1903. Surprisingly, Cu_2MnAl is ferromagnetic even though none of its elements are ferromagnetic on their own [2, 18].

The large number of alloys in the family of Heusler compounds allows for a large degree of tuneability of the properties of the alloys. Many Heusler compounds have a

T_C above room temperature, and have tuneable spin polarization at the Fermi level, important for magnetic tunnel junction devices [13]. Heusler alloys found use as semiconductors in thermoelectric [19], peizoelectric [20] and optoelectric devices [21]. There are two stoichiometry varieties of Heusler compounds: Full-Heusler alloy and half-Heusler alloys.

1.1.1 Half-Heuslers XYZ

Half-Heuslers compounds (XYZ) where X & Y are transition metal elements and Z is a main group element have the space group F$\bar{4}$3m (#216). The most electropositive element is denoted by X, and the most electronegative element by Z. Half-Heuslers where Y is a rare earth or alkaline element are also possible. The name half-Heusler alloys come from containing half the amount of X atoms when compared to full-Heusler alloys.

The Wyckoff positons for the XYZ compound are as follows: 4a (0, 0, 0), 4b (1/2, 1/2, 1/2), and 4c (1/4, 1/4, 1/4). The X, Y, and Z atoms in an ordered crystal structure occupy specific Wyckoff sites. However, there can be a variety of ordering of X, Y, and Z on the 4a, 4b, and 4c sites [2, 22]. The half-Heusler structure can be realized as 3 interpenetrating face centered cubic (fcc) lattices. A rock salt substructure is formed by the atoms at 4a and 4b sites (Fig 1.3a), and the 4a and 4c sites form a zinc blende structure like GaAs (Fig 1.3b). Figure 1.3c shows the half-Heusler structure. In magnetic half-Heusler alloys, the magnetic moment typically resides at the 4c sites.

1.1.2 Full-Heuslers X_2YZ

Full-Heusler compounds (X_2YZ) come in two variants: the one that belongs to the space group Fm$\bar{3}$m (225) is called a regular full-Heusler, and the one from the F$\bar{4}$3m (216) space group is called an inverse full-Heusler. Similar to half-Heuslers the X and Y atoms are typically 3d transition metals, and the Z atom is a main group element.

Full-Heuslers can be thought of as 4 interpenetrating FCC lattices. The regular full-Heuslers (Fm$\bar{3}$m) have atoms Y & Z located at Wyckoff sites 4a (0, 0, 0), 4b (1/2, 1/2, 1/2) and the X atoms on sites 4c (1/4, 1/4, 1/4) and 4d (3/4, 3/4, 3/4). Figure 1.4a shows the regular full-Heusler structure, which can be thought of as two

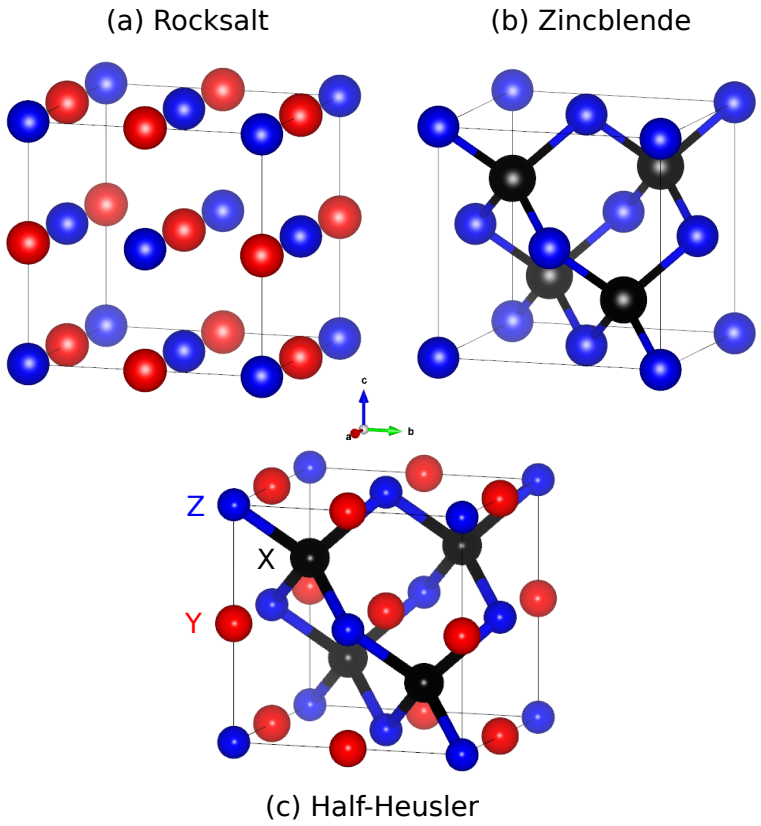

Figure 1.3: (a) A rock salt structure with 4a (blue) and 4b (red) Wyckoff positions, and (b) a zinc blende structure with 4a (blue) and 4c (black) Wyckoff positions. Merging the two substructures yields (c), the half-Heusler structure depicting the 4a (blue), 4b (red), and 4c (black).

interpenetrating zinc blende structures, one formed by the 4a and 4c sites, and one from the 4b and 4d sites [2]. Figure 1.4b depicts an inverse full-Heusler ($F\bar{4}3m$), which is formed when X occupies the 4a & 4d sites, Y the 4c sites, and Z the 4b sites.

A tetragonal distortion of the inverse full-Heusler lowers the symmetry to $I\bar{4}m2$ (119). Figure 1.4c shows the conventional unit cell; its relationship to the cubic structure is shown by the dotted cell in Fig 1.4b. $I\bar{4}2m$ has a D_{2d} point group and therefore the structure is capable of hosting skrymions [17]. The X atoms are located on the Wyckoff positions 2b (0, 0, 1/2) and 2c (0, 1/2, 1/4), Y atoms are found on the Wyckoff positions 2d (0, 1/2, 3/4), and Z atoms on Wyckoff positions 2a (0, 0, 0).

Magnetic Heusler compounds typically follow the Slater-Pauling rule [23, 2, 24]. The Slater-Pauling rule determines the magnetic moment from the average valence

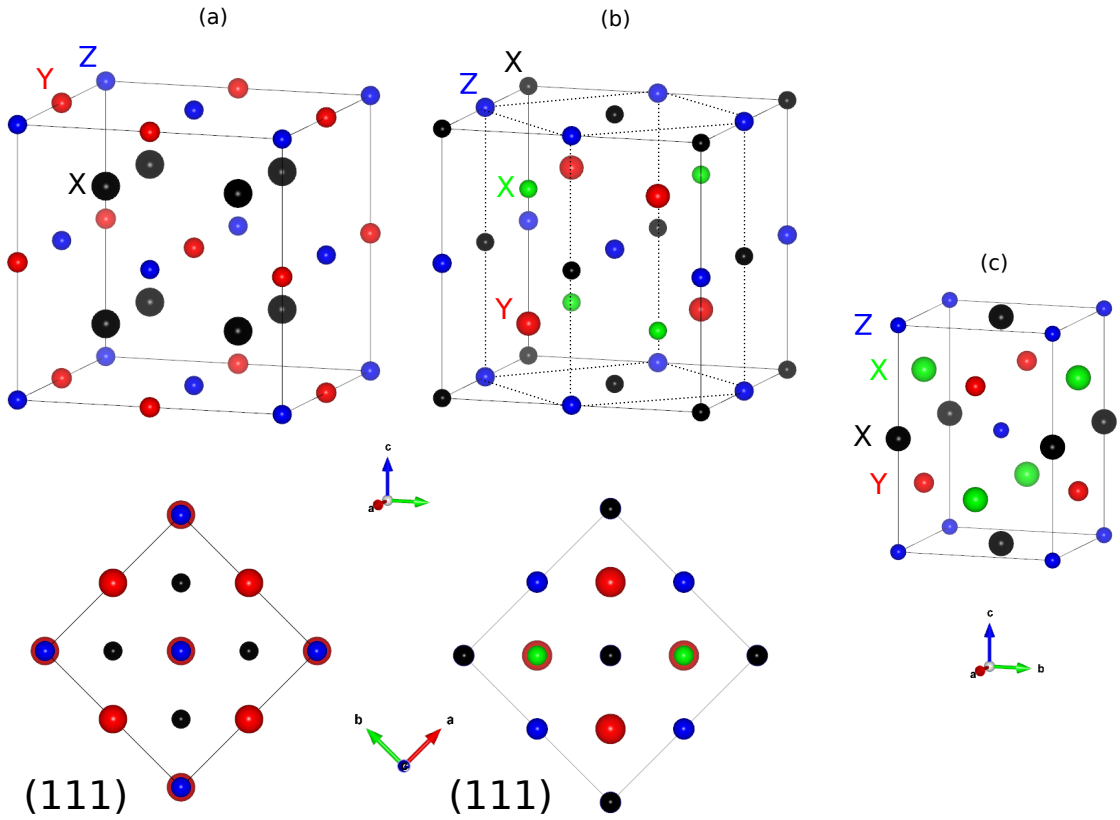

Figure 1.4: The regular full-Heusler structure (a) depicting Wyckoff positions at 8c (black), 4a (blue), and 4b (red). The inverse full-Heusler structure (b) depicting the Wyckoff positions 4a, and 4c (black and green), 4d (blue), and 4b (red). The tetragonal inverse full-Heusler structure (c) can be visualized from the dotted lines in (b), but is elongated along the c direction. The view along the (111) direction is below the isometric view of the Heusler structures.

electron number N_V per atom. Typically, atoms with a low number of valence electrons ($N_V \leq 8$) have localized moments, where atoms with $N_V \geq 8$ give rise to itinerant magnetism. Heusler compounds follow structures found with low numbers of valence electrons. The magnetic moment for many full-Heuslers is described by,

$$m_{\mathrm{X_2YZ}} = N_V - 24. \tag{1.1}$$

Figure 1.5 shows how the magnetic moment varies linearly with increasing N_V [2]. Compounds with a N_V lower than 24 are less common, and Mn based full-Heuslers are predicted to be in this region.

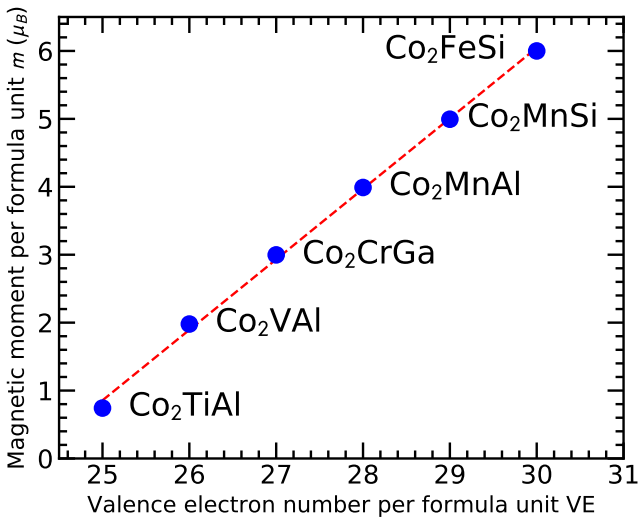

Figure 1.5: Some Co_2 based Heusler compounds showing the magnetic moment is proportional to the valence electrons, and is in good agreement with the Slater-Pauling curve (stylized from [2]).

1.2 Hexagonal Ni_2In-type structure

The Ni_2In-type structure belong to the spacegroup $P6_3/mmc$ (#194) [25, 26, 27]. The atoms are distributed on 3 sets of Wyckoff positions: 2a (0, 0, 0), 2c (2/3, 1/3, 1/4), and 2d (1/3, 2/3, 3/4), shown in Figure 1.6. In the case of XYZ alloys, the X atoms occupy the 2a sites, that form sparse (001) planes, Y and Z atoms occupy the 2c and 2d sites that form denser (001) planes.

1.2.1 Magnetic bubble: biskyrmion

NiMnGa is an example of a material with a Ni_2In-type structure. It has attracted recent interest due to reports of observations of so-called biskyrmions, even though the crystal structure is centrosymmetric [28]. However more careful analysis of TEM measurements of biskyrmions in NiMnGa recently show that they are not skyrmions but are simple magnetic bubbles—cylindrical magnetic domains. The large magnetocrystalline anisotropy due to the hexagonal crystal structure contributes to the stability of these domains.

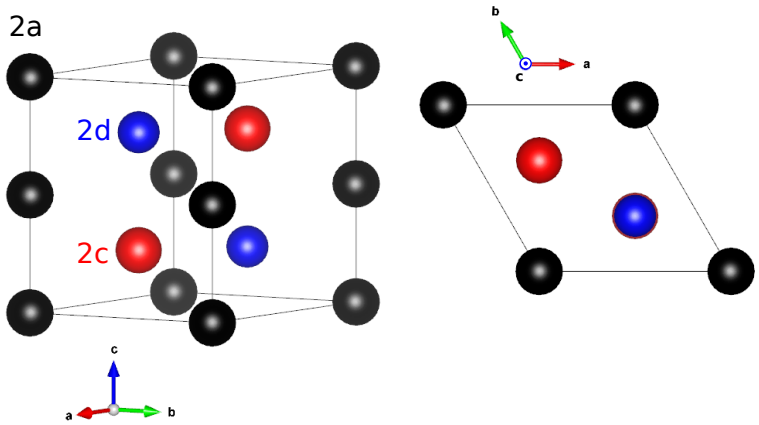

Figure 1.6: Ni_2In-type structure with Wyckoff positions 2a (black), 2c (red), and 2d (blue).

1.2.2 Magnetic Refrigeration: Permament magnets

Magnetic refrigeration occurs when an external changing magnetic field causes heat to flow from a material due to the induced change in entropy of the spins in a magnetic material. The underlying phenomena is termed the magnetocaloric effect (MCE) [29]. The magnetocaloric effect gained notarity when Giauque used the effect to achieve a temperature of 250 mK [30] from proposals outlined by Debye [31]. Progress in superconducting materials brought the onset of magnetic refrigeration closer to room temperature. By 2001, devices that used the superconducting materials were superseded by permanent magnets in applications related to the MCE [32].

Bulk MnCoGe has been explored as a potential material for magnetic refrigeration [33, 34]. MnCoGe undergoes a martensitic transformation between a TiNiSi-type Pnma structure, and the Ni_2In-type $P6_3/mmc$ structure. This martensitic transformation produces a large MCE in MnCoGe and occurs at a temperature between the T_C's of the two phases. In this dissertation, the $Mn_\alpha CoGe$, $Mn_\alpha RhGe$ and Mn_2IrGe are found have a Ni_2In-type structure and can be compared to bulk MnCoGe. Structural changes in these films are observed with annealing, although no Pnma phase was found.

1.3 Hexagonal P$\bar{6}$2m and orthorhombic Ima2 structures

The hexagonal Fe_2P-type P$\bar{6}$2m structure is also an interesting structure because of its large MCE [35, 36]. Figure 1.7 shows the Fe_2P-type structure whose Wyckoff sites are 1b (0, 0, 1/2), 2c (1/3, 2/3, 0), 3f (x_1, 0, 0) and 3g (x_2, 1/2, 0), where x_1 = 0.2582 and x_2 is 0.5912. The Fe_2P-type P$\bar{6}$2m structure transitions to a TiFeSi-type Ima2 structure at high temperature [37, 38]. Unlike the centrosymmetric Fe_2P-type structure, the TiFeSi-type structure is a non-centrosymmetric crystal structure (C_{2v}).

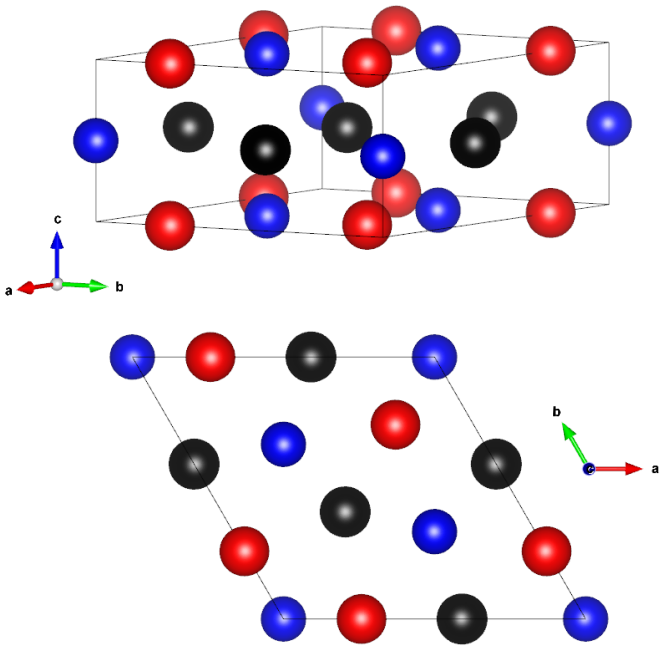

Figure 1.7: Fe_2P-type structure with atoms X (black on 3g sites), Y (red on 3f sites) and Z (blue on 1b and 2c sites).

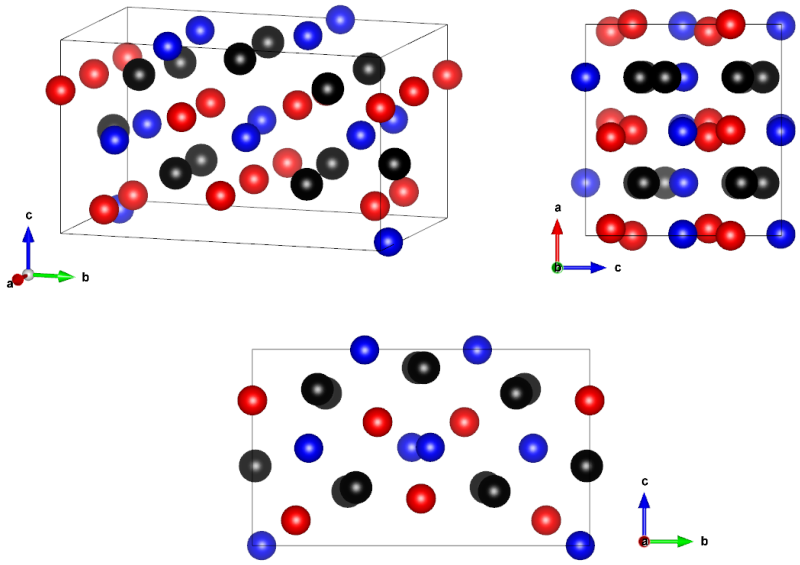

Figure 1.8: TiFeSi-type (Ima2) structure with atoms X (black), Y (red) and Z (blue).

Chapter 2

Film Deposition

Physical vapour deposition (PVD) is a broad term used to describe the family of deposition techniques that transfer atoms or molecules from a source via a vapour, to the desired substrate. PVD techniques are typically used to generate thin films that range in thickness from subnanometers to micrometers [39]. In magnetron sputtering the vapour is generated within a vacuum by a plasma environment [39, 40].

Sputtering is used to deposit a wide variety of materials. The base pressure of the chambers are several orders of magnitude higher than techniques such as molecular beam epitaxy. This enables samples and targets to be changed quickly.

2.1 Sputtering deposition

Magnetron sputtering deposition is PVD that uses a solid target (source) that is negatively charged. When exposed to a bombardment of positively charged ions, atoms are ejected from the target in a low vacuum Ar environment between 0.5–30 mTorr and are deposited on a substrate as depicted in Figure 2.1. Sputtering deposition takes advantage of an electrode system to attract ionized atoms towards the target. The target (cathode) is set to a negative potential, while the substrate table, and the rest of chamber (anode) are held at ground.

The potential difference between the target and the table causes an avalanche of free electrons to migrate towards the anode. The electrons ionize the Ar that generates more electrons that ionize more of the Ar. The ionized Ar is accelerated towards the target and ejects target particles from the surface into the vacuum. The impact from the Ar causes secondary electrons to be ejected from the target, this helps to facilitate a self sustaining plasma of ionized Ar. A set of magnets placed behind the target create a magnetic field that concentrates a torodial shaped plasma above the surface of the target; this increases the effective ionization by allowing a lower pressure of ionizing gas. Lower pressure increases the λ_{fp} of sputtered atoms

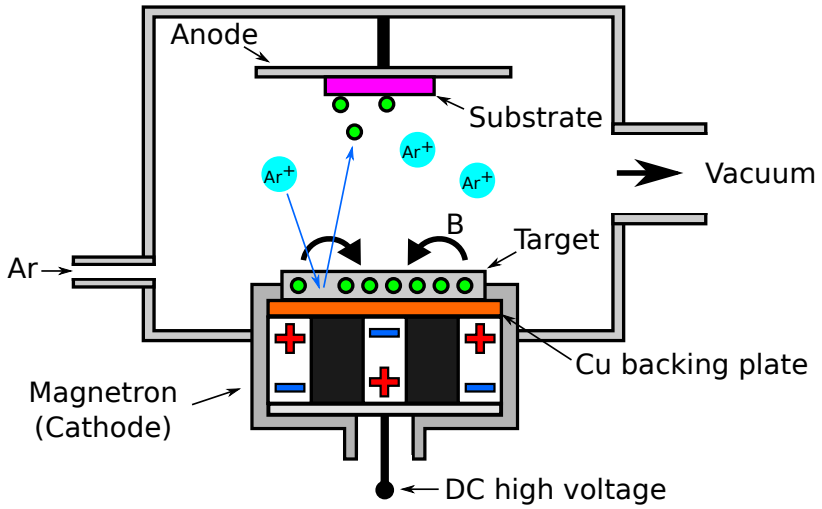

Figure 2.1: Outline of DC magnetron sputtering within an Ar gas environment. Desired target material atoms (small green circles) are ejected from Ar ions colliding with the target; the ejected atoms deposit onto the substrate (magenta).

from the target, and increases the sputter rate [41, 40, 39].

A Corona Vacuum Coater V3T sputtering deposition system was used to grow all samples in this dissertation. It is configured to hold up to five magnetron sputter target sources. The system has DC magnetron power supplies. Each sputter target has a tunnel to guide the flux towards the sputtering table in order to limit contamination to other regions of the chamber. Each tunnel can have a mask afixed to the exit opening to change the deposition profile [41]. Each tunnel was equipped with constant deposition masks for all growths presented in the dissertation. Figure 2.2 shows the configuration and layout of the system that was used. The substrates are adhered to the rotating table with 3M vacuum double-sided tape at a distance of 13.3 cm from the table centre, where the flux is most uniform [41]. The Mn, Co, Ni and Ge targets were purchased from Lesker, and the Rh and Ir were donated by Jeff Dahn.

Sputter target deposition calibrations shown in Appendix A were performed with powers less than 75 W to limit the thermal stress on the Mn target to in order to avoid cracking, as per the instructions from the target manufacurer, *Kurt J. Lesker* [42]. The Mn target was always set to a DC sputtering power of 75W when co-depositing, with Co, Rh, Ir, and Ge.

The deposited samples were calibrated by measuring the mass over 1 cm $\times$ 1

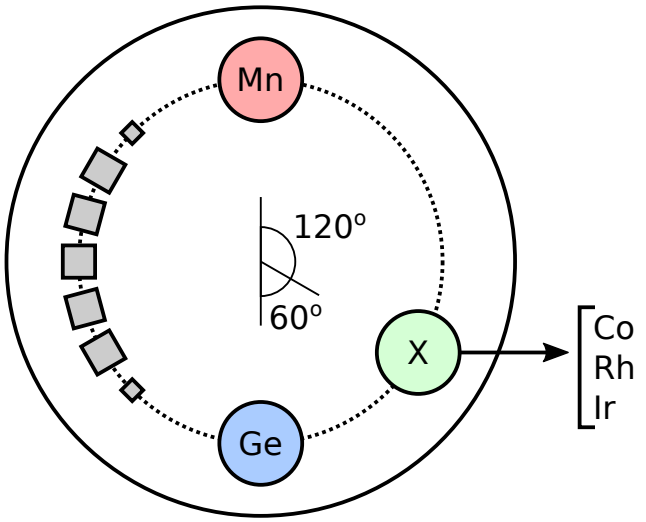

Figure 2.2: Corona Vacuum Coater V3T system configuration used for depositing Mn, {Co, Rh, Ir}, and Ge compounds. The samples (squares) are situated so they pass over the middle of the targets as the circular table is rotated.

cm area over the duration of the depososition, as identified as the smaller substrate samples shown in Fig 2.2. The deposited mass was compared with the deposition rates of each target over the time used for sputter deposition (see Appendix A). The measured mass of deposited samples is within 3% of the projected mass from deposition rates.

2.2 Substrate preparation

The Si(001) wafer substrates used throughout this dissertation were purchased from *Prolog semicor Ltd.*. These wafers are 100.0 ± 0.5 mm in diameter, 380 ± 25 μm thick, having one polished side and were doped with boron (resistivity 5-10 Ohms $\cdot$ cm). Si(001) wafers were cut into 20 mm $\times$ 20 mm pieces, which will be referred to as substrates throughout this work.

To remove hydrophobic contaminants and organics from the surface, the substrates were sonicated in acetone and methanol baths for 15 minutes each. To avoid recoating the samples with the organic contaminants during removal from the bath, water was gently added to the methanol bath after sonication to allow the contaminants to flow over the edges of the beaker.

2.2.1 SiO_2 diffusion barrier

Substrates were cleaned prior to thermal treatments as described in §2.2, then heat treated in a dry furnace at 900°C for 5 hours to *grow* an estimated 300 nm SiO2 layer on the exposed surfaces. The thickness is estimated by the color of the thermally treated substrate and compared against a SiO_2 film colour chart [43]. Samples were post cleaned before sputter deposition.

2.3 Rapid thermal annealing RTA

As deposited samples were annealed in a *Modular Process Technology RTP600s* rapid thermal annealer. The RTA operates at temperatures between 200°C-1200°C, and is water cooled. Annealing took place in a Ar environment. The rapid thermal annealer was configured to reach the desired temperatures within 20 s (15–35 °C/s), while holding the set temperature for the duration of the anneal; the samples were then cooled to room temperature. The temperatures are recorded using a Type-K thermal couple which has an error 0.75% for temperatures over 0°C. However, the thermal couple is only in contact with the sample annealing plate, so there is likely a small temperature gradient between the sample and the thermocouple. Because of this limitation there is no way to know precisely the temperature of the sample. The display is only accurate to 1°C, however, the error will be quoted from the Type-K thermocouple as a guide. The annealing temperature varied from 300°C±2°C-700°C±5°C, with annealing times as low as 2 minutes to as long as 47 minutes. Long annealing times were broken into 15 minute segments to accommodate operating conditions of the rapid thermal annealer.

Chapter 3

Methods, and Techniques

3.1 X-ray diffraction (XRD)

X-ray Diffractometry (XRD) is a non-destructive technique used to identify phases of a crystallographic material [44, 45]. Peaks in the diffraction pattern arise from constructive interference of X-rays scattered from atomic planes. The collection of peaks can be used to determine the crystal structure and lattice parameters of the material. The relationship between plane spacing d and the scattering angle θ is given by Bragg's Law see Figure (3.1a) [46, 47, 48]. Constructive interference occurs when the path length difference for X-rays scattered from neighbouring planes, $2d\sin\theta$, is an integer multiple of wavelengths, λ. The angle of the n-th order diffraction peak is given by Bragg's Law.

$$2d\sin\theta = n\lambda. \tag{3.1}$$

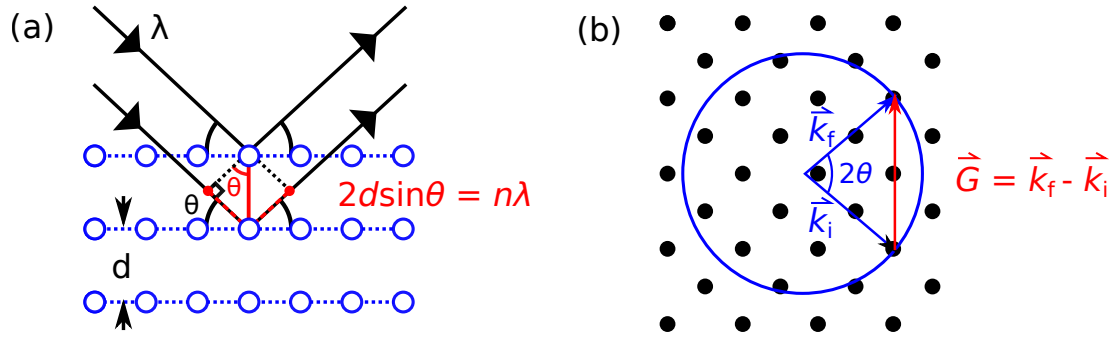

Figure 3.1: Bragg's law showing constructive interference by d spaced planes (a), and an Ewald's sphere demonstrating the conditions for constructive interference, which occurs when the difference between the incident wavevector k_i and outgoing wavevector k_f is equal to a reciprocal lattice vector, G.

A polycrystalline material is a collection of randomly oriented crystallites. In the case of XRD, a sample is irradiated with K_α X-rays, which undergo scattering from the electron distribution. Figure 3.1b shows incident X-rays with incident wavevector

k_i that scatter from a family of atomic planes. A sphere with radius of k_i, called an Ewald sphere, defines the outgoing wavevectors k_f that satisfies conservation of energy. When the scattering vector, $q = k_f - k_i$ equals a reciprocal lattice vector, $\vec{G}$, the scattered X-rays interfere constructively. The reciprocal lattice vector can be written as $|\vec{G}| = \dfrac{2\pi n}{d}$. This allows Bragg's law to be rewritten as,

$$|\vec{G}| = 4\pi \frac{\sin\theta}{n\lambda}. \tag{3.2}$$

The scattered X-ray intensity can be calculated by $I \propto |S(\vec{G})|^2$, where $S(\vec{G})$ is defined as the structure factor:

$$S(\vec{G}) = \sum_n f_n(\vec{G}) \exp\Big(i\vec{G} \cdot \vec{r}_n\Big), \tag{3.3}$$

where the sum is over the position of all atoms in the unit cell, $\vec{r_n}$. The form factor $f_n(\vec{G})$ is the Fourier transform of the scattering potential $V_n(\vec{G})$,

$$f_n(\vec{G}) = \int V_n(\vec{r}) \exp\left(-i\vec{G} \cdot \vec{r}\right) \mathrm{d}^3 r\,. \tag{3.4}$$

where V_n is proportional to the charge density of the n^{th} atom.

Intensity measurements were acquired on a *Siemens D500 Diffractometer*. $\mathrm{K}_{\alpha 1}$ and $\mathrm{K}_{\alpha 2}$ X-rays have wavelengths λ=154.0596 pm and 154.4426 pm respectively. They are generated from a Cu source, with a setting of 30 kV, and 35 mA. The detector is outfitted with a monochromator to allow $\mathrm{K}_{\alpha 1}$ and $\mathrm{K}_{\alpha 2}$ X-rays to pass through. The geometry shown in Figure 3.2 depicts a standard $\theta - 2\theta$ scan setup. The detector and source are 200.5 mm away from the centre of the sample stage. The source is fixed while the detector rotates about the sample stage as shown in the figure. The sample stage rotates about the the axis drawn and labelled in the figure to achieve the typical geometry of a $\theta - 2\theta$ scan. Two sets of slits are added in front of the source X-rays to control the beam divergence and as a consequence the X-ray footprint on the sample. An antiscattering slit is placed after the sample to prevent stray X-rays reaching the detector, and followed two detector slits to limit the divergence of the beam that strikes onto the detector.

The 0.3° divergence and antiscattering slits where used give a full beam divergence of 0.3° (or a radial beam divergence of 0.15°). The 0.15° detector slits were used for all measurements.

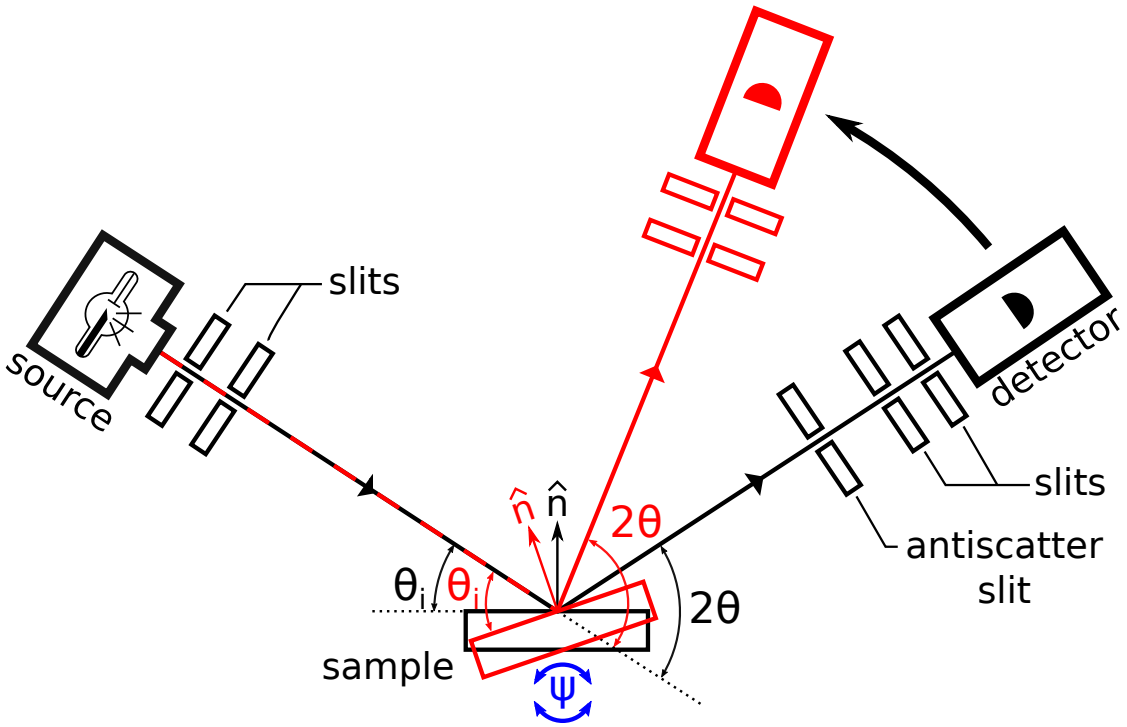

Figure 3.2: XRD setup depicting X-ray source, detector, sample stage, and slits for $\theta - 2\theta$ scans.

One difficulty encountered with the $\theta - 2\theta$ scan was the large Si(004) diffraction peak at 2θ=69.9°. This peak overshadows any peaks generated by the film. The Si(004) peak can be reduced by offsetting θ_i by ψ=2°. Another alternative to eliminate substrate contributions is to run the system in a grazing angle mode.

3.1.1 Grazing angle XRD: Thin-film characterization

Thin-films can be measured using grazing angle XRD (GAXRD), as shown in Figure 3.3. GAXRD fixes the incident beam at a low angle and does *not* allow the sample stage to rotate unlike a $\theta - 2\theta$ XRD scan while the detector rotates about the sample. The technique is utilized to control the X-ray penetration depth, allowing GAXRD to test for variations in the crystal structure across the depth of the film, or to exclude contributions from the substrate. Grazing incident angles requires a large sample surface area due to the large foot print of the X-ray beam, f_p. The f_p is dependent upon the slit configuration, and incident angle. The GAXRD measurements in this

dissertation were collected at a grazing angle of 6.0° for the higher count rate compared to lower grazing angles (Fig 3.4) and suppressing contributions of the forbidden Si(002) peaks from defect substrates. These peaks were uncovered in θ_i=3.0°, and 4.0° and are likely due to multiple scattering of the X-rays. The slits were chosen to be 0.3° such that the f_p was 10 mm, which is smaller than the length of the 20 mm × 20 mm samples.

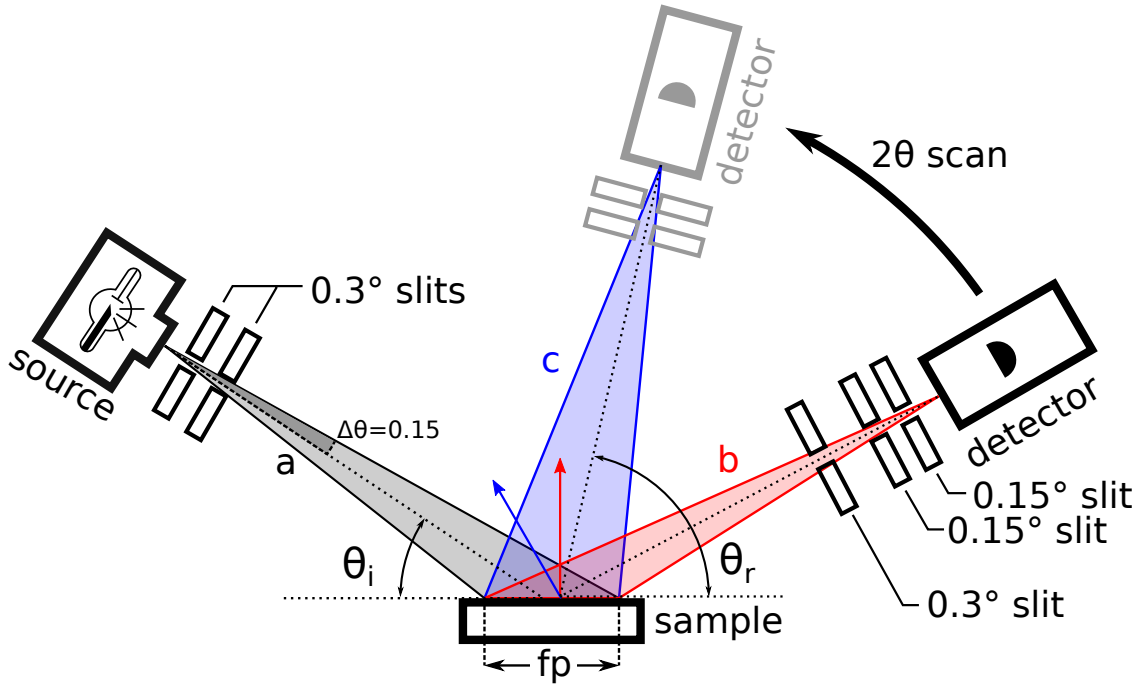

Figure 3.3: Glancing angle XRD configuration. Source is fixed (a), while the detector swept through a 2θ scan. The red, and blue arrows depict the normals to the planes that the detector is sensitive to for the two detector positions shown.

The penentration depth can be estimated using the mass attenuation coefficient μ/ρ of the sample (Eq. (3.6)) [49], where μ is the attenuation coefficient, and ρ is the density. The mass attenuation coefficient is a weighted average of mass attenuation coefficients of the elements $(\mu/\rho)_i$, with atomic weight w_i in the material. The attenuation length of X-rays can be estimated by $L = \mu^{-1}$, and the effective depth that the X-rays penetrate into the sample is given by $z_L = 0.5L \sin\theta$. The reflected X-ray intensity I can be calculated from the incident intensity I_0,

$$I = I_0 \exp\left[-\left(\mu/\rho\right)\rho z_L\right]. \tag{3.5}$$

$$\left(\frac{\mu}{\rho}\right) = \sum_i w_i \left(\frac{\mu}{\rho}\right)_i \tag{3.6}$$

Densities were estimated by weighing of the films grown on 1 cm × 1 cm Si substrate with a *Sartorious SE2 Micro Balance*, and measuring the film thickness with a *Vecco Dektak contact profilometer*. At an angle of 6° the penetration depth of MnCoGe and MnRhGe are 319 nm, and 245 nm respectively. This implies that samples must be grown thicker than these values for an incident angle of 6° in order to avoid potential contributions from the substrate. All samples in this work were grown between 475 nm and 550 nm thick.

Table 3.1: Mass attenuation coefficient values from NIST at 8 keV.

Element	μ/ρ (cm^2/g)
Mn	2.734E+02
Co	3.248E+02
Ge	6.890E+01
Rh	1.915E+02
Ir	1.914E+02

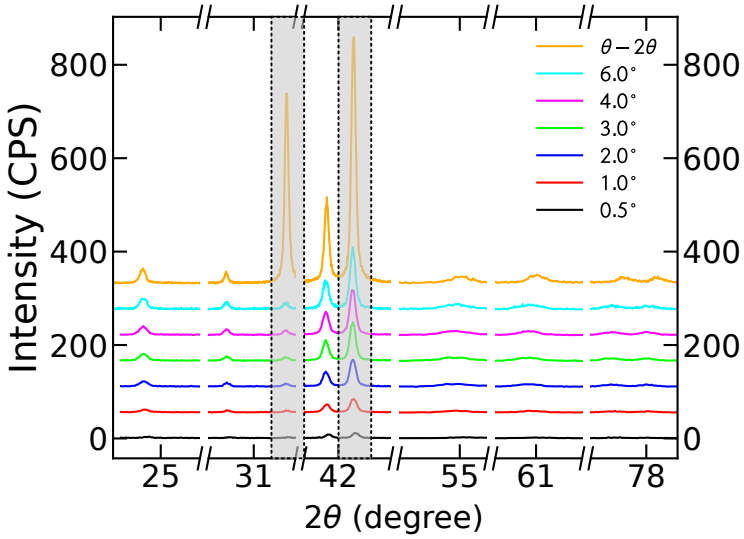

Figure 3.4: Varying incident angle θ_i in GAXRD measurements gives insight into the preferred orientation of a textured $Mn_{2.0}RhGe$ film. The shaded regions highlight the (002) and (110) peaks whose intensity varies greatly with grazing angle relative to the other crystallographic orientations.

3.2 Magnetic characterization

Magnetic measurements were performed using a *Physical Properties Measurement System* (PPMS) by Quantum Design, equipped with a *P500 AD/DC Magnetometry System* (ACMS). Temperatures were varied between 5 K and 300 K in fields up to 9 T. Figure 3.5 shows the sensor configuration for measuring magnetic properties. A sample is oscillated through a set of coils in a first order gradiometer configuration that reduce background contributions [50]. The changing magnetic flux created by the oscillating sample induces an EMF in the coil.

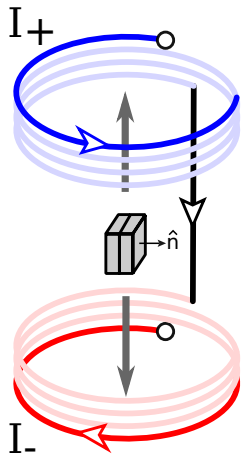

Figure 3.5: PPMS detector coil configuration. Sample oscillates between the two sets of coils within a constant applied field $\mu_0 H_{\text{ext}}$ to and measures the derivative of the magnetization via current loops. The samples are stacked in sets of 2 or 3 with their normal, $\hat{n}$, perpendicular to the oscillation to measure the in-plane magnetization.

3.2.1 Magnetic hysteresis

A full hysteresis loop is measured starting from a demagnetized state. This state was achieved by cooling the samples through T_C in zero external magnetic field. The magnetization is then measured at fixed temperatures from $\mu_0 H_{\text{ext}} = 0$ to fields well above the saturation field. The magnetization at this point is referred to the saturation magnetization, M_{sat}. This first branch of the $M - H$ loop is referred to as the virgin curve, and gives insight into the magnetization reversal mechanisms. The field is then swept through a complete cycle (from +9 T to -9 T and back). The point on the loop at zero field corresponds to the remanent magnetization, M_R. The field required to reverse the magnetization is the coercive field, H_C.

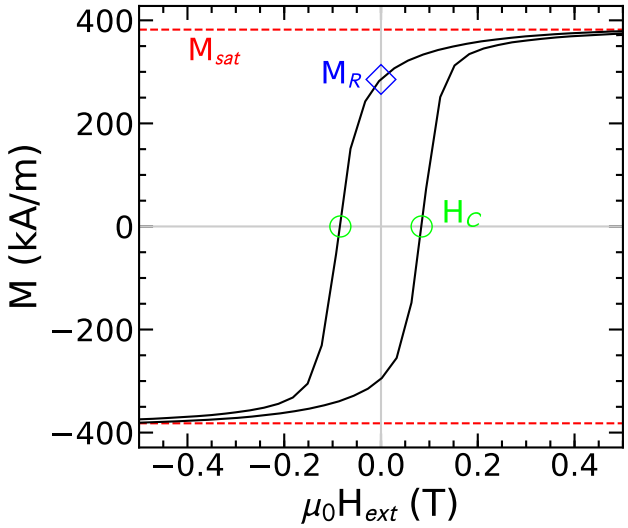

Figure 3.6: Magnetic hysteresis curves depicting saturation magnetization, remanent magnetization, and coercive field.

Stoner-Wolfharth single domain model

The Stoner-Wolfharth single domain model describes the magnetic reversal of a single magnetic domain with uniaxial magnetocrystalline anisotropy [3]. If a particle's width is smaller than a value of the order of the domain wall width, the spin in the particle will form a single domain (see Fig 3.7a). Figure 3.7b shows a field $\mu_0 H_{\text{ext}}$ applied at an angle θ_0 with respect to the easy axis of the particle. The field causes M to kant away from the easy axis. The angle between H and M is θ. Figure 3.8a shows a schematic diagram of a collection of single domain particles, with a random distribution of easy axes. Averaging the hysteresis loops of an ensemble of all possible domain configurations $\{\theta_0\}$ gives the hysteresis loop shown in Fig 3.8b, where

$$\begin{aligned} M_R &= 0.5 M_{\text{sat}}, \\ \mu_0 Hc &\approx 1.0 \frac{K_u}{M_{\text{sat}}}. \end{aligned} \tag{3.7}$$

Equation (3.7) allows one to estimate the uniaxial magnetocrystalline anisotropy, K_u, from the hysteresis loop of a suitable material.

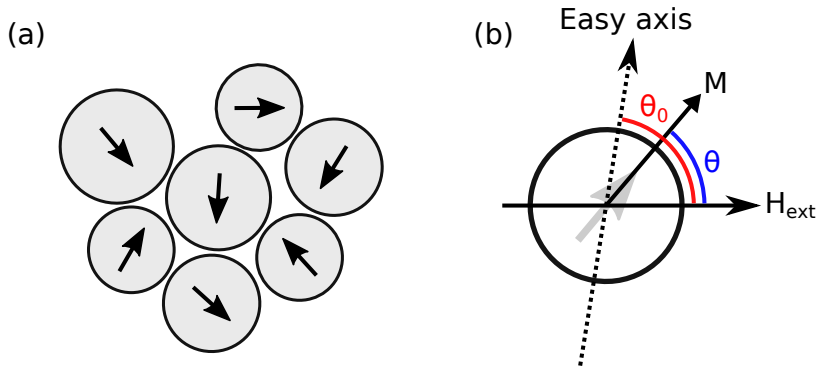

Figure 3.7: (a) An ensemble of magnetic single domain particles, where the spins align along the particle's easy axis. (b) An external field applied at an angle θ_0 with respect to the easy axis; this causes the moment to kant towards H_{ext} at angle θ with respect to the field.

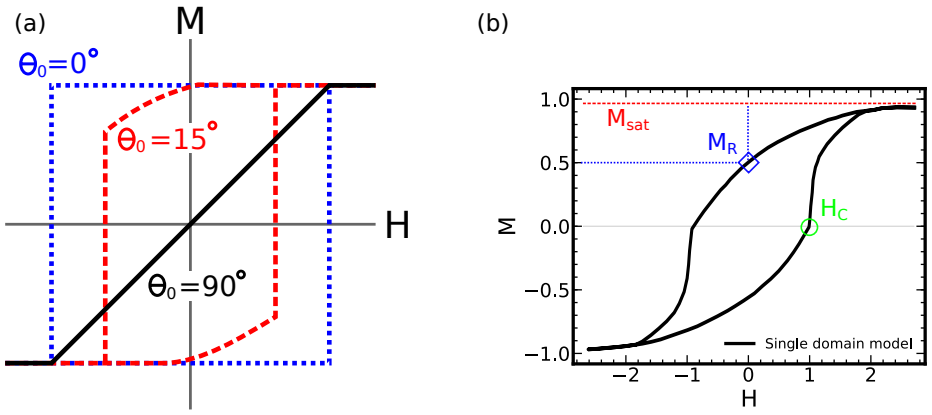

Figure 3.8: (a) A set of single domain hysteresis loops from the Stoner-Wohlfarth model as a function of θ_0. The average of these loops yield the $M - H$ curve (b) for a random distribution of uniaxial single domain particles.

3.2.2 Remanent magnetization measurement

Remanent magnetization measurements are done between T=5 K–300 K. The sample is cooled to 5 K, then saturated by $\mu_0 H_{\text{ext}}$=9 T. After the external field is relaxed to zero, the magnetic moment is recorded upon heating to temperatures above T_C (when possible).

The T_C is determined from the T where M_R goes to zero. This point is determined from the knee in the $M_R - T$ graph by fitting two straight lines to portions of the curve on either side of the knee, as shown in Figure 3.9.

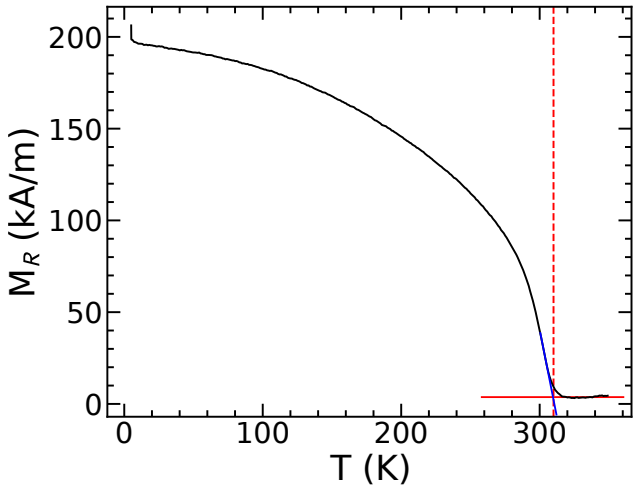

Figure 3.9: A typical $M_R - T$ curve, with the estimate of the Curie temperature T_C highlighted by the red dashed line.

Chapter 4

$Mn_\alpha CoGe$ alloys

The first set of ternary compounds we explored was $Mn_\alpha CoGe$. Although MnCoGe is a well known magnetocaloric material, little is known about $Mn_{2.0}CoGe$. The choice of substrate was motivated in part by previous work on the growth of B20 compounds on Si(111). The B20 silicides and germanides, which included MnSi, MnGe, and FeCoSi, and FeCoGe, can be grown epitaxially on Si(111) due to good lattice matching [51]. A Mn or Fe seed layer reacts with the Si substrate to form stable B20 layer that is an excellent template for subsequent silicide or germanide growth. A MnSi layer is stable on Si(111) for temperatures below 400 °C. The germanium based alloys are lattice matched to Si(001), and therefore Si(001) was hoped to behave in a similar fashion for these Heuslers. Furthermore, given Si(001) is well lattice matched to the germanium-based Heusler alloys, it may be a good substrate for epitaxial growth of these materials. It is therefore of interest to understand the stability of the Heusler/Si(001) interface in order to explore the possibility of epitaxial growth. Furthermore Si(001) substrates have the added advantage that no diffraction peaks exist bellow the (004) peak at $2\theta = 69.9$ °.

This thesis explored growth on SiO_2, which is not lattice matched to the materials grown. The growth on Si(001) without the oxide is the subject of future work. Films were grown on room temperature substrates, which produced amorphous layers. These were subsequently annealed in a rapid thermal annealer in order to produce polycrystalline films. However, the native oxide, which is approximately 2 nm thick, was not a suitable diffusion barrier. Annealing over 500 °C caused significant diffusion of Mn into Si to create MnSi, and $MnSi_{1.7}$ alloys, as shown in Fig. 4.1 for a sample annealed at 700 °C for 4 minutes. The evidence of these $MnSi_{1.7}$ films is based on work on MnSi/Si(111) and the Mn-Si phase diagram. As you anneal MnSi, Mn diffuses in Si to form so called layered silicide $MnSi_{1.7}$ alloys. A variety of phases are identified: MnSi, $MnSi_{1.7}$, and Ge. In the case of Co_2FeSi sputtered on SiO_2/Si(001), the

problem of diffusion of transition metal into the substrate was solved by depositing on commericially available Si on insulator (SOI) wafers [52, 53]. SOI has an embedded 60 nm thick SiO_2 layer, burned in oxide (BOX) layer, covered by a 40 nm thick Si(001) layer. The BOX layer can be created by either wafer bonding or using an oxygen ion beam to embed oxygen into the substrate, after the substrate is annealed to create a SiO_2 embedded layer. The Co and Fe reacted with the top Si(001) layer, but the embedded burned oxide (BOX) 60 nm thick SiO_2 layer prevented further diffusion. Motivated by the result, we prepared a ∼300 nm SiO_2 layer which can be readily created by heating wafers in an oxygen atmosphere on Si(001) at 900 °C for 5 hours. These thick SiO_2 layers were good diffusion barriers. The wafers were supplied by *Prolog*.

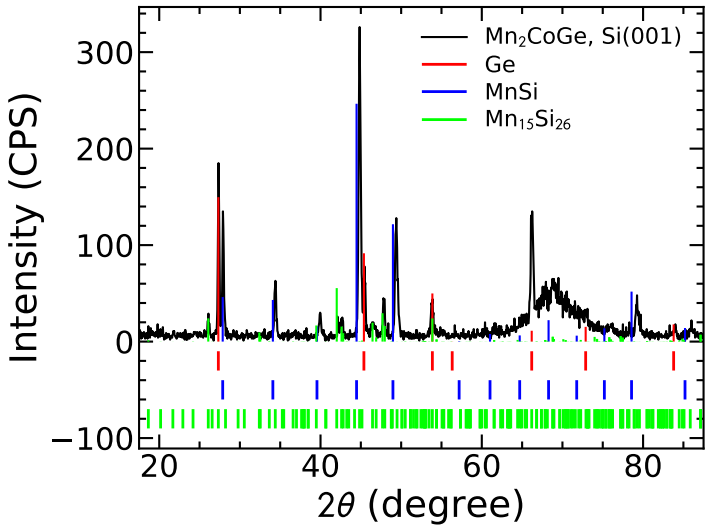

Figure 4.1: XRD pattern of $Mn_{2.0}CoGe$ grown on the native oxide on a Si(001) wafer and annealed at 700 °C, showing diffusion into Si(001) substrate. The sample has peaks identified as MnSi, $MnSi_{1.7}$, and Ge.

The thin films were grown on 300 nm SiO_2/Si(001) and annealed in a rapid thermal annealer (RTA) an Ar environment, at temperatures between 300°C and 900°C. The RTA was set to ramp to the target temperature within 20 seconds, while samples were allowed to cool to room temperature before XRD measurements. Samples were annealed for 2 minutes at a time, and then measured by XRD. The temperature was gradually increased between heating cycles until a stable crystallographic phase was

achieved. If no suitable phases were found, then new samples were annealed for longer time at lower temperatures to see if any crystallographic phase would form.

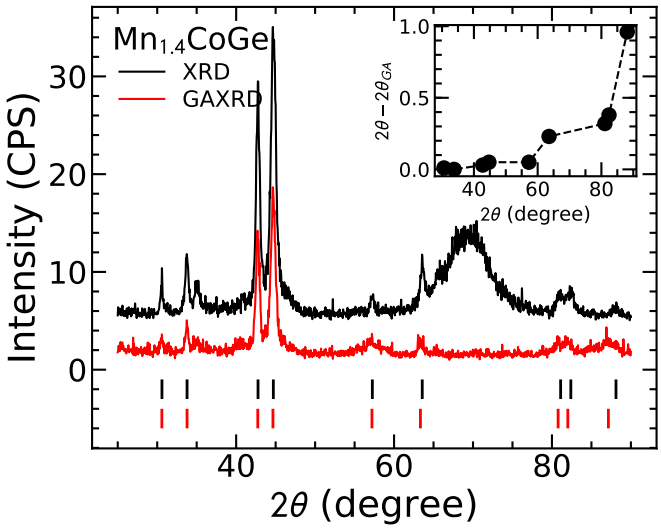

Figure 4.2: XRD patterns for $Mn_{1.4}CoGe$: $\theta - 2\theta$ (black), and GAXRD (red); The substrate 100 peak can still be seen at 69.9 ° in the $\theta - 2\theta$ XRD pattern even though the sample angle is offset by 2°. The inset shows peak location differences between GAXRD and XRD.

Traditional $\theta - 2\theta$ XRD measurements proved to be problematic since diffraction peaks near the Si(004) peak proved to be important for phase identification of the intermetallic germanides. The Si(004) peak could be substantially reduced by offsetting the sample angle ψ by a few degrees. However, as the intensity of the Si(004) substrate is significantly more intense than the polycrystalline film peaks, the shoulder of this peak is still clearly visible in the diffraction data. The shoulder makes the peak fitting difficult, and therefore we also collected diffraction measurements in a glancing-incidence geometry, as shown in Fig. 4.2. Unexpectedly, the GAXRD measurements showed small difference in the peak positions as compared to the conventional $\theta - 2\theta$ XRD measurements, as shown in the inset of Figure 4.2.

The GAXRD 2θ peaks were found at smaller angles than the XRD measurements, and this difference became more appreciable with increasing 2θ. This discrepancy is not due to misalignment of the X-ray machine: Fig 4.3 shows that the GAXRD and XRD of a Si powder sample are in good agreement. Sample misalignment also

cannot explain a 1° difference between GAXRD and XRD measurements: this would require a vertical sample misalignment of 1 mm. Strain, however, does account for the difference. As 2θ increases, the GAXRD peaks correspond to interatomic planes whose normal is further and further from the film normal. The films crystallize at high temperature, and the bonding with the substrate is also expected to change when this occurs. Then as the film cools, the difference in thermal expansion coefficients between the film and substrate would be expected to induce a strain in the film. Given the larger thermal expansion coefficients for metals as compared to Si (see table 4.1), the cooling would be expected to give rise to an in-plane tensile strain. The film along the perpendicular direction would then most likely experience compressive strain through the Poisson ratio of the material [46].

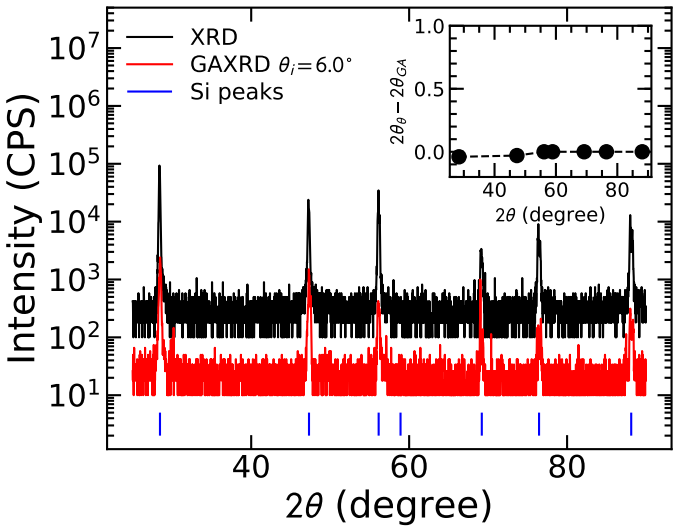

Figure 4.3: XRD and GAXRD patterns for powder Si. The inset shows peak location differences between GAXRD and XRD.

The majority of samples annealed for short durations (less than 30 minutes) were susceptible to in-plane tensile strain effects. However, the $Mn_\alpha RhGe$ study did not exhibit the strained behaviour, *i.e.* there was no discrepancy in peaks between the techniques; an example of this is shown in Fig 4.4. However, unlike the $Mn_\alpha CoGe$ samples, these two samples delaminated during the annealing and therefore the substrate would not be able to induce a strain in this case.

Figure 4.5 shows in-plane tensile strain acting on crystallites whose normal is not

Table 4.1: Thermal expansion coefficients

Element	α_{thermal} $(10^6\,\text{m/m}^{-1}\text{K}^{-1})$
Si	3-5
SiO_2	5.9
Mn	22
Co	12
Ge	6.1
Rh	8
Ir	6.4

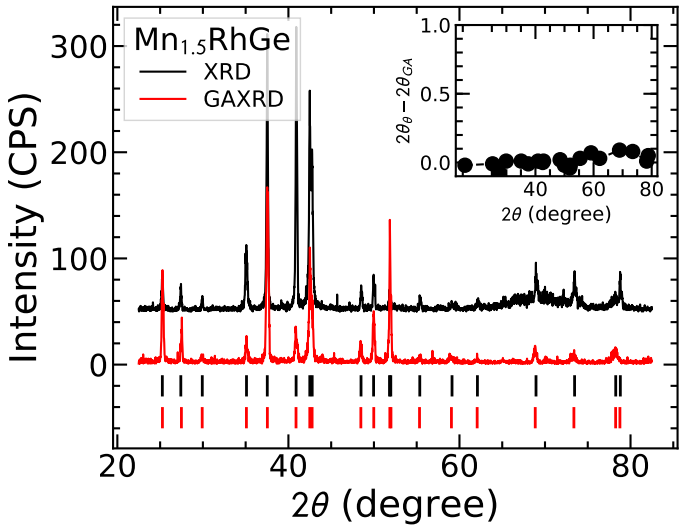

Figure 4.4: XRD patterns for $Mn_{1.5}RhGe$: $\theta - 2\theta$ (black), and GAXRD (red); show consistent peak positions, but still exhibit differences in intensity. The substrate 100 peak can still be seen at 69.9 ° in the $\theta - 2\theta$ XRD pattern.

parallel to the substrate normal. The in-plane and out-of-plane strain $\epsilon_{\parallel}$ and $\epsilon_{\perp}$ respectively are related to Poisson's ratio ν for an isotropic medium [54].

$$\frac{\epsilon_{\perp}}{\epsilon_{\parallel}} = -\frac{1-\nu}{2\nu} \tag{4.1}$$

To model the shift in the GAXRD peaks, we define a deformation field $\vec{u}(\vec{x})$ due to the substrate induced stress. This field relates the points in the film $\vec{x}$ before deformation to $\vec{x}'$ after deformation, $\vec{u}(\vec{x}) = \vec{x}' - \vec{x}$. The vector $\vec{d}_{lmn}$ defined to point along the normal of a given family of lattice planes (lmn) with a magnitude

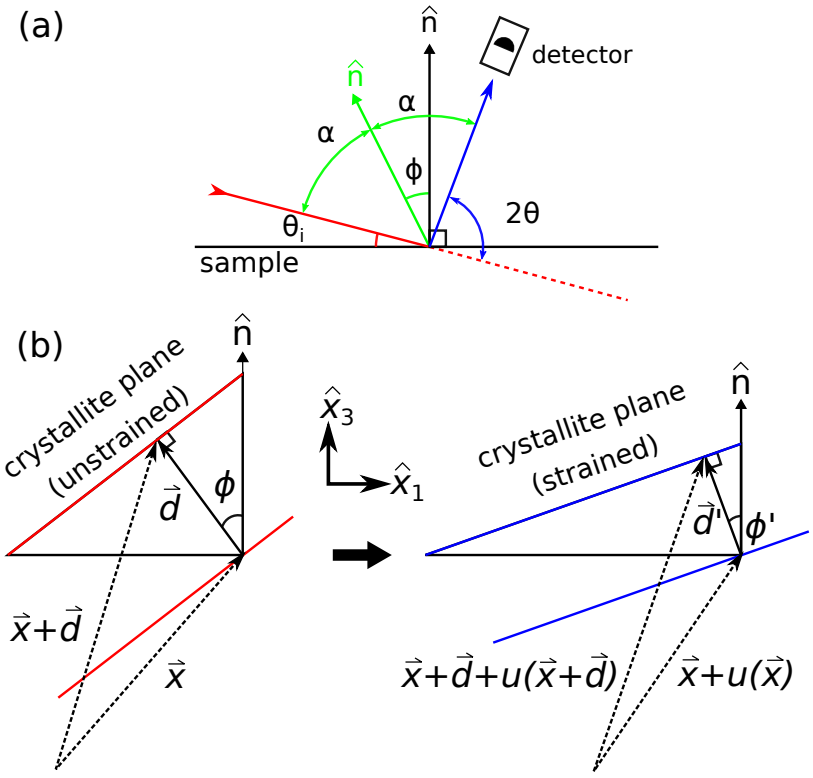

Figure 4.5: (a) Geometry of a crystallite whose normal is offset from the substrate normal, where θ_i is the incident grazing angle and 2θ is the angle of the detector. (b) Unstrained planes, spaced by d, on the left (red) whose normal is offset by ϕ from the normal of the substrate. Strained planes, spaced by d', on the right (blue) whose normal is offset by ϕ', with strain transformation applied to the Cartesian grid. The function $u(x)$ is defined as the strain tensor, that deforms the planes.

corresponding to the plane spacing:

$$\vec{d}_{lmn} = \frac{2\pi}{|\vec{G}|}\hat{G}_{lmn}, \tag{4.2}$$

where $\vec{G}_{lmn}$ is the reciprocal lattice vector. This is used to calculate $\vec{d'}$, the plane spacing as a function of orientation in the strained film. The d-spacing $\vec{d'}$ in the strained case can be written as $\vec{d'} = \vec{d} + \vec{u}(\vec{x} + \vec{d}) - \vec{u}(\vec{x})$, where $\vec{u}(\vec{x} + \vec{d})$ can be expanded in a Taylor series, and i, and j index the components of the vectors,

$$u_i(x_j + d_j) \cong u_i(x_j) + \sum_j \frac{\partial u_i}{\partial x_j} d_j. \tag{4.3}$$

The component of $\vec{x}$ along the film normal, $\vec{n}$, is given as x_3 (see Fig 4.5). With the

Taylor expansion of $\vec{u}(\vec{x}+\vec{d})$, $\vec{d'}$ can be rewritten as,

$$(\vec{d'}-\vec{d_i}) = \sum_j \frac{\partial u_i}{\partial x_j} d_j. \tag{4.4}$$

The magnitude of $\vec{d'}$ is obtained from

$$d'^2 = \vec{d'}\cdot\vec{d'} = \sum_i d_i^2 + 2\sum_{i,j} d_i \frac{\partial u_i}{\partial x_j} d_j + \sum_{i,j,j'} \frac{\partial u_i}{\partial x_j}\frac{\partial u_j}{\partial x_i} d_j d_{j'}. \tag{4.5}$$

The third term is of the order $(\partial u_k/\partial x_l)^2$ and is small and can be neglected. The second term can be rewritten as,

$$\sum_{i,j} d_i \left(\frac{\partial u_i}{\partial x_j} + \frac{\partial u_j}{\partial x_i}\right) d_j,$$

which is related to the strain tensor is defined as $\epsilon_{ij} = \frac{1}{2}\left(\frac{\partial u_i}{\partial x_j} + \frac{\partial u_j}{\partial x_i}\right)$ [55]. The substrate does not induce a shear, therefore the off-diagonal terms of ϵ_{ij} are zero. The geometry laid out in Figure 4.5 shows that we only care about ϵ_{11} and ϵ_{33}. These can be relabelled as,

$$\epsilon_{\parallel} = \epsilon_{11},$$
$$\epsilon_{\perp} = \epsilon_{33}.$$

Equation 4.5 becomes

$$d'^2 = d^2 + 2d_1^2\epsilon_{\parallel} + 2d_3^2\epsilon_{\perp},$$

which in terms of the angle between $\vec{d}$ and $\vec{n}$ is

$$\frac{d'^2}{d} = 1 + 2\epsilon_{\parallel}\sin^2\phi' + 2\epsilon_{\perp}\cos^2\phi'. \tag{4.6}$$

To compare the GAXRD and XRD measurements we calculate the plane spacing $d'(\phi)$ to the plane spacing of planes parallel to the substrate $d'(0)$,

$$\frac{d'(\phi)}{d'(\phi=0)} = \left(\frac{1+2\epsilon_{\parallel}\sin^2\phi + 2\epsilon_{\perp}\cos^2\phi}{1+2\epsilon_{\perp}}\right)^{\frac{1}{2}}. \tag{4.7}$$

From Fig 4.5 the angle ϕ can be related to the experimental parameter 2θ:

$$\phi = \theta - \theta_{\mathrm{i}}.$$

It is not possible to extract both $\epsilon_{\parallel}$ and $\epsilon_{\perp}$ from a fit to $d'(\phi)/d'(0)$, as demonstrated by a Taylor series expansion for small strain and small ϕ,

$$\frac{d'(\phi)}{d'(\phi=0)} \approx 1 + (\epsilon_{\parallel} - \epsilon_{\perp})\phi^2. \tag{4.8}$$

The data in Fig 4.6 show a fit to $d'(\phi)/d'(0)$ measured for the $Mn_{1.4}CoGe$ sample. The fit gives a value $\epsilon_{\parallel} - \epsilon_{\perp} = 0.069 \pm 0.01$. Comparing the bulk and films values for a and c parameters, the $\epsilon_{\perp}$ is approximately -0.0123, which gives a value of $\nu = 0.52 \pm 0.04$.

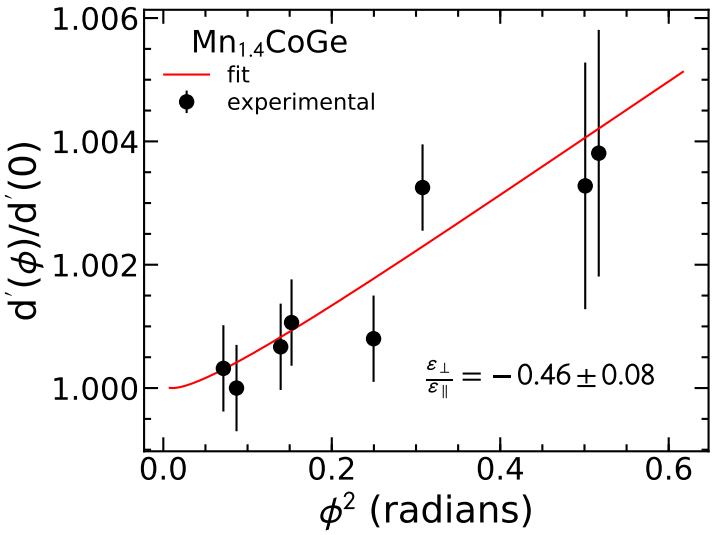

Figure 4.6: The ratio of d-spacings, $d'(\phi)/d'(0)$ for $Mn_{1.4}CoGe$. Where $d'(\phi)$ is the plane spacing from GAXRD, and $d'(0)$ is the spacing obtained from XRD.

This analysis explains the discrepancy between the measured peak positions and the calculated values at high angle.

4.1 $Mn_{2.0}CoGe$

The $Mn_{\alpha}CoGe$ GAXRD data were fit using *Rietica* Rietveld refinement software with the samples annealed at 400 or 500 °C are shown in Fig 4.7. $Mn_{1.0}CoGe$, $Mn_{1.4}CoGe$, and $Mn_{2.0}CoGe$ have a $P6_3/mmc$ Ni_2In-type structure (see Fig 1.6). Refinement of the distribution of Mn and Co on the Wyckoff sites is not possible, because Mn and Co have similar form factors $f(\vec{G})$. The lattice parameters are extracted from the refinement software, as shown in Table 4.2.

Table 4.2: $Mn_\alpha CoGe$ parameters extracted from XRD. Thin-film lattice parameters varied by ±0.005 Å.

Alloy	Temp. (K)	Time (min)	a (Å)	c (Å)	d_{grains} (nm)
MnCoGe (bulk $P6_3/mmc$)			4.10	5.36	
$Mn_{1.0}CoGe$	375	15m	4.02	5.21	24.7
$Mn_{1.4}CoGe$	500	4m	4.05	5.29	25.6
$Mn_{2.0}CoGe$	500	2m	4.08	5.31	27.1

Figure 4.7 shows the GAXRD data for a $Mn_{2.0}CoGe$ sample annealed at 400 °C for 2 min. A fit reveals a Ni_2In-type structure ($P6_3/mmc$), not the expected tetragonal structure. However, in the case of the related $Mn_\alpha PtSn$ alloy, the Heusler alloy would also not form when α=2. An inverse tetragonal phase was obtained by reducing α to 1.4, which produced vacancies on the Mn sites [17]. Therefore we applied the same approach to $Mn_\alpha CoGe$ and grew samples with α={1.0, 1.4}.

The samples in this dissertation were measured to be 3% of the projected deposition based on the sputter deposition rates for the magnetron targets. Additional verification of the various stoichiometries showed conflicts between electron dispersive spectroscopy (EDS), wavelength dispersive spectroscopy (WDS) and inductively coupled plasma mass spectrometry (ICP-MS). The EDS measurements were collected on a *Hitachi S4700 SEM/EDS* and showed up to 50% stoiciometry discrepancies over various excitation voltages 5, 10, 15 and 20 kV. The atomic % ratios were attempted over a variety of combinations of the characteristic X-rays produces from the K, L and M shells but did not yield consistent results. The WDS measurements were carried out using a *JEOL JXA-8200 Electron Probe Micro-Analyzer (EPMA)* and showed similar inconsistencies. The ICP-MS measurements lacked the Ge standard for our set of materials for calibration purposes. The measurements were more inconsistent than EDS and WDS, for Co and Rh concentrations vary from -20%-+50% with respect to Mn, while Ir varied by 500%. Therefore, the sputter deposition mass references samples for each run were used as the metric for stoichiometry accuracy, as it was consistent within the error of the sputter deposition.

Initially we investigated $Mn_{1.0}CoGe$ since this is well studied in bulk form [56, 57, 58, 59, 60]. Bulk MnCoGe at room temperature forms an orthorhombic P*nma* structure [61, 58, 59, 60]. MnCoGe undergoes a martensitic transformation at T_M=355 K

to a $P6_3/mmc$ structure. However, this transition is sensitive to defects and can be lowered below room temperature by a number of ways. A reduction in Mn produces vacancies on the Co-sites in $Mn_{0.975}CoGe$, which forms a $(Mn_xCo_{1-x})(Co_x\square_{1-x}Ge)$ structure with T_M=293 K, where $\square$ is a vacancy. The $P6_3/mmc$ phase can also be formed by reducing the Co content: $Mn_{1.07}Co_{0.92}Ge$ has a T_M=210 K. Co vacancies also stabilize the hexagonal phase in $Mn_xCo_{1-x}Ge$. A surplus of Mn in $Mn_{1+x}CoGe$ is also found to lower T_M. Some combination of these defects in $Mn_{1.0}CoGe$ films likely explain why Fig 4.7a shows that the films have a Ni_2In-type hexagonal structure instead of the low temperature $Pnma$ phase reported in bulk samples. Thin-film $Mn_{1.0}CoGe$ annealing posed challenges, as the sample would delaminate after heating over 400 °C. The sample would only form the high temperature Ni_2In-type phase over a 10 °C window about 375 °C ± 5 °C.

By increasing the Mn content in $Mn_\alpha CoGe$ up to $\alpha = 2$, no phase separation or deviation from $P6_3/mmc$ was observed. The XRD patterns in Fig 4.7 only show the $P6_3/mmc$ Ni_2In-type structures. The $P6_3/mmc$ phase was found to be robust to defects based on the X-ray refinements. The $Mn_\alpha CoGe$ samples were found to have a large number of vacancies within the unit cell. A third stoichiometry $Mn_{1.4}CoGe$ was also sputter deposited to check between the Mn concentrations of $1 \leq x \leq 2$. The $Mn_{1.4}CoGe$ annealed at 500 °C for 2 minutes, yielded another Ni_2In-type structure (see Fig 4.7) that has no qualitative differences with the $Mn_{1.0}CoGe$ and $Mn_{2.0}CoGe$ compounds. The $Mn_{1.4}CoGe$ did not show any indication of a tetragonal structure [17].

There are only small differences in XRD peak intensities between the 3 sets of samples, $\alpha = 1.0, 1.4, 2.0$.

4.2 Magnetic characterization

Annealed samples were cut to 5.6 mm × 5.6 mm ± 0.01 mm^2 squares, stacked in groups of 2, or 3, and placed in the PPMS sample holder[1]. Samples were cooled to 5 K before prior to any measurements. Magnetic hysteresis curves were generated over a range -9 T $\leq H_{ext} \leq$ +9 T. After a hysteresis curve was measured at 5 K, the

[1]Sample holder opening was sealed with Kapton tape to prevent samples from falling in the chamber upon cooling

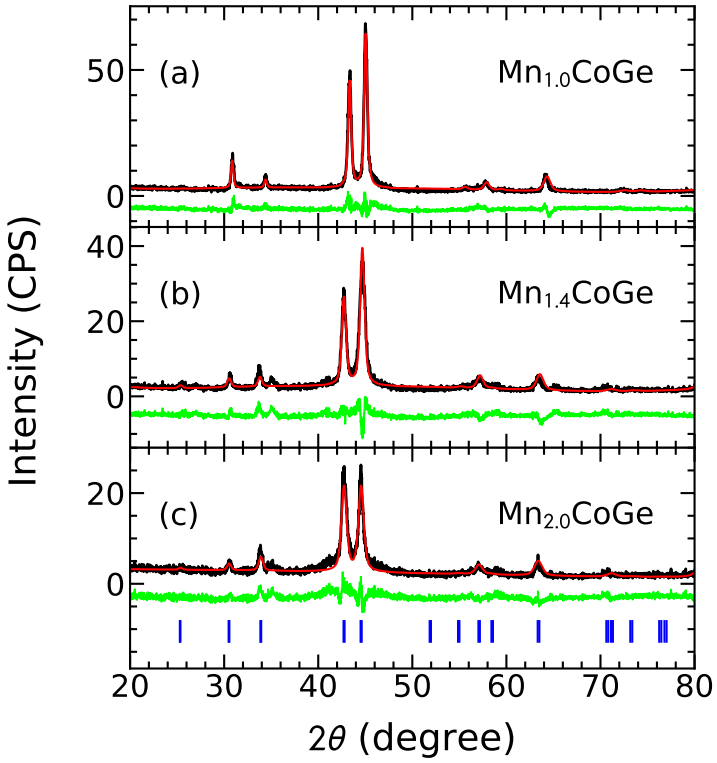

Figure 4.7: GAXRD refinements for $Mn_{1.0}CoGe$, $Mn_{1.4}CoGe$, and $Mn_{2.0}CoGe$ thin-films that were annealed for 2 minutes at 400 °C for (a) and (b), while (c) became stable at 500 °C for 2 minutes. These patterns were measured for a dwell time of 17 s. Crystal phase identified as $P6_3/mmc$ Ni_2In-type structure, with peak locations shown in (c).

applied field was lowered from H_{ext}=9 T to zero. The remanent magnetization, M_R, was then measured on warming. The warming was interrupted at regular intervals to perform a hysteresis loop between +9 T and -9 T. The intermediate hysteresis loops did not have a noticeable impact on the measurements of M_R.

The $M-H$ loops shown in Fig 4.8 reveal that $Mn_\alpha CoGe$ $P6_3/mmc$ alloys are relatively soft ferromagnets. The coercive field H_C increases as the concentration of Mn increases. The saturation magnetization of $Mn_{1.0}CoGe$, M_{sat}=377 kA/m corresponds to 1.48 μ_B/f.u. in formula units (f.u.): this is 51-53 % of the value expected from measurements of well ordered bulk samples, M_{sat}=2.78–2.91 μ_B/f.u. [62]. This could be explained by the disorder in the films, since the magnetic moment only resides on

the 2a sites [63]. Vacancies on 2a sites range from 20%-30% in the $Mn_{\alpha}CoGe$ samples, and so could explain the majority of this difference.

Table 4.3: $P6_3/mmc$ Magnetic properties of $Mn_{\alpha}CoGe$

Alloy	M_{sat} (kA/m)	M_{sat} (μ_B/f.u.)	$\mu_0 H_C$ (T)	T_C (K)
MnCoGe (bulk)†	400	2.78-2.91‡	0.036	269
$Mn_{1.0}CoGe$	377	1.48	0.027	260
$Mn_{1.4}CoGe$	422	2.03	0.079	274
$Mn_{2.0}CoGe$	345	1.88	0.089	259

†Magnetic measurements at a temperature of 2 K [64, 65]
‡M_{sat} including vacancies [62]

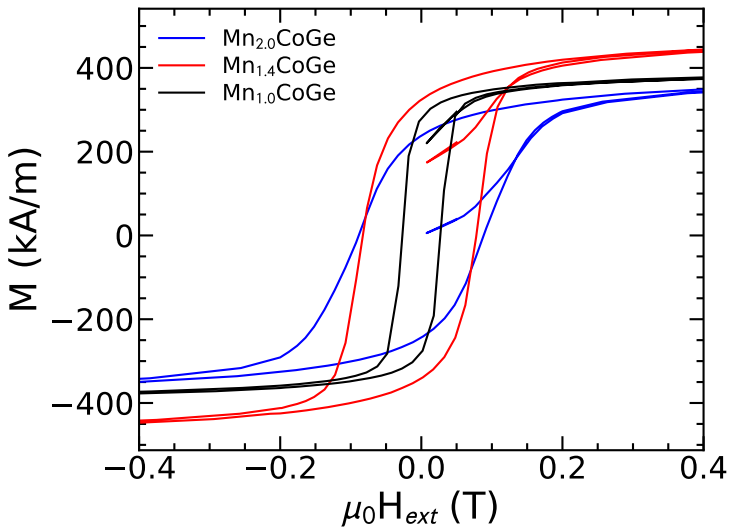

Figure 4.8: Magnetic hysteresis curves for $Mn_{\alpha}CoGe$ ternary compounds at 5 K. Magnetization per volume shows M_{sat} for $Mn_{1.0}CoGe$, $Mn_{1.4}CoGe$ and $Mn_{2.0}CoGe$ to be 377 kA/m 422 kA/m, and 345 kA/m respectively. The coercive fields for $Mn_{1.0}CoGe$, $Mn_{1.4}CoGe$ and $Mn_{2.0}CoGe$ are $\mu_0 H_C$=0.0272 T, $\mu_0 H_C$=0.079 T and $\mu_0 H_C$=0.089 T respectively.

Figure 4.9 shows the $M_R - T$ curves for the $Mn_{\alpha}CoGe$ ternary compounds. The M_R-T curve for $Mn_{2.0}CoGe$ has a T_C=259 K. The M_R-T for $Mn_{1.4}CoGe$ shows a similar curve with a drop in M_R near the T_C of $Mn_{1.4}CoGe$, which is about 274 K. However, the M_R does not go to zero over the measurement range of the instrument. This additional component is due to a secondary phase, although this phase is not

apparent in the diffraction patterns (see Fig 4.7). Figure 4.11 shows that the secondary phase can be prevented from forming with suitable annealing. In the case of $Mn_{2.0}CoGe$ annealed at 500 °C, the secondary phase is evident from the non-zero M_R for $T > T_C = 259\,K$. The same is true for $Mn_{1.4}CoGe$ annealed at 400 °C. However, by selecting a lower annealing temperature of 400 °C for $Mn_{2.0}CoGe$, the secondary phase does not form. It is plausible that for a given sample, multiple phases with the same crystal structure, but different stoichiometry, coexist.

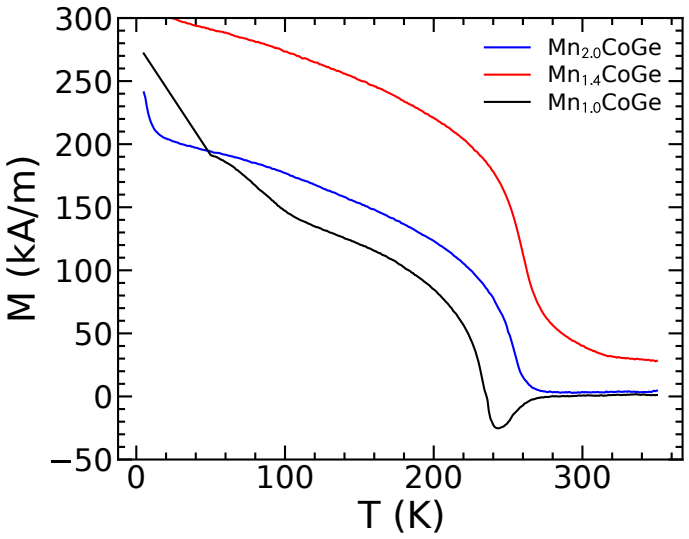

Figure 4.9: Remanent magnetization M_R versus temperature. $Mn_{2.0}CoGe$ (blue) has an expected remanent magnetization curve with T_C at 259 K, $Mn_{1.0}CoGe$ (black) M_R curve shows evidence of ferrimagnetic-like behaviour, with a T_C of 259 K, and $Mn_{1.4}CoGe$ (red) showing evidence of a secondary phase.

Unlike the $Mn_{2.0}CoGe$, $Mn_{1.4}CoGe$, or bulk MnCoGe, the $Mn_{1.0}CoGe$ thin-film sample in Fig 4.9 shows a ferrimagnetic-like behaviour. The typical M-T curve for a ferrimagnet is shown in Fig 4.10) [3]. A naïve hypothesis is that the $Mn_{1.0}CoGe$ material is ferrimagnetic, where there are two opposing magnetic sublattices within the crystal structure [3]. Given $Mn_{1.0}CoGe$, and $Mn_{2.0}CoGe$ have the same T_C, we tested the hypothesis by assuming one of the *apparent* magnetic sublattices has the same M_R curve as $Mn_{2.0}CoGe$ M_R. The saturation was rescaled and subtracted from the M_R of the $Mn_{1.0}CoGe$. The scaling factor was adjusted to give a physically plausible $M_R - T$ for the second sublattice (see Fig 4.12). However, the $M_R - T$ curves

from the result have different T_C values, which would mean the two sublattices have different T_C's. This is likely not possible due to the strong exchange interaction between sublattices.

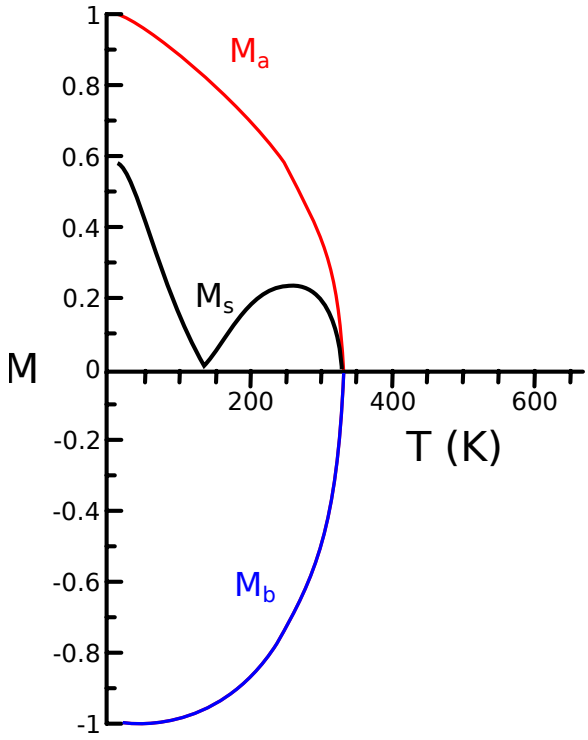

Figure 4.10: A recreated representation of a N-type ferrimagnetic $M_R - T$ curve from Chikazumi et al. [3], showing the compensation point T_{cmp}, where the two magnetic sublattices (red, and blue) sum to zero, and the Curie temperature T_C of the system. The dashed black lines is representative of the situation such that the applied field is low enough where the magnetization doesn't reverse above T_{cmp}.

An alternative hypothesis for thin-film $Mn_{1.0}CoGe$ is that the system contains ferromagnetic grains that are antiferromagnetically coupled to their neighbours [66]. An arrangement of smaller moment grains antiferromagnetically coupled to larger moment grains would create an artificial ferrimagnet, but where the two sets of grains could have different T_C's. Excess Mn at the grain interfaces could act as the mechanism for the antiferromagnetic coupling of grains [67]—as Mn is known to be antiferromagnetic. Antiferromagnetic coupling could be the result of deposited Mn at the end of the growth due to slower cool down rates for the Mn sputter target compared to Co and Ge. The targets continue to deposit material as the machine is slowly turned off, and deposits an additonal 3% mg/cm^2. Furthermore the deposition rates

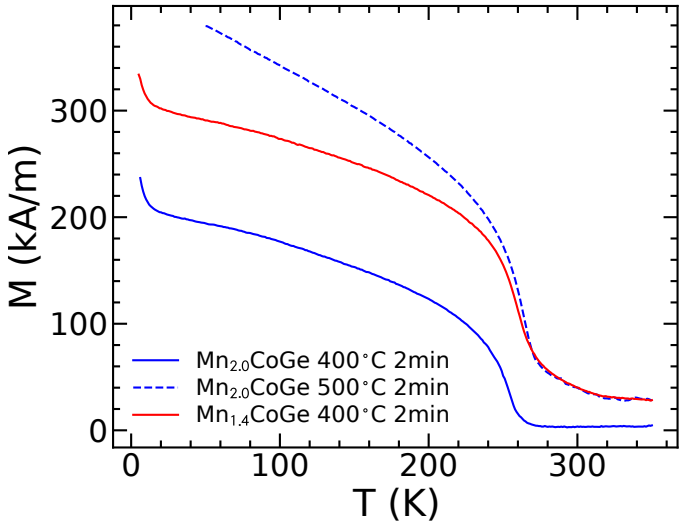

Figure 4.11: The removal of soft a secondary magnetic phase by annealing $Mn_{2.0}CoGe$ to 500 °C for 2 minutes. This is compared to $Mn_{2.0}CoGe$ and $Mn_{1.4}CoGe$ annealed at 400 °C for 2 minutes.

are not calibrated at low powers and therefore the relative flux rates may vary as the targets are turned off. Co and Ge target sputter deposition rates may not follow a linear deposition trend at low operating powers, thus do not sputter predictably during cool down, and could lead to an excess of Mn at the surface or the formation of CoO when sample is removed from the chamber [68]. Another issue with $Mn_{1.0}CoGe$ was the fact that the films break into pieces if the annealing temperature was above 400 °C. Samples annealed for longer times below 400 °C resulted in a diffraction pattern with amorphous peaks.

In summary, the thin-film $Mn_{\alpha}CoGe$ did not exhibit the expected tetragonal structure as predicted by DFT [13, 17]. However, $Mn_{\{1.0,1.5,2.0\}}CoGe$ compounds formed to a hexagonal Ni_2In-type structure, similar to bulk MnCoGe due to defects. The diffraction patterns of the $Mn_{\alpha}CoGe$ show no obvious differences due to variances in the amount of Mn. Magnetic characterization was comparable to MnCoGe bulk, with lower M_{sat} possibly due to defects on the 2a Wyckoff sites. The $Mn_{1.0}CoGe$ sample shows ferrimagnetic-like behaviours, that is possibly due to antiferromagnetic coupling of magnetic grains.

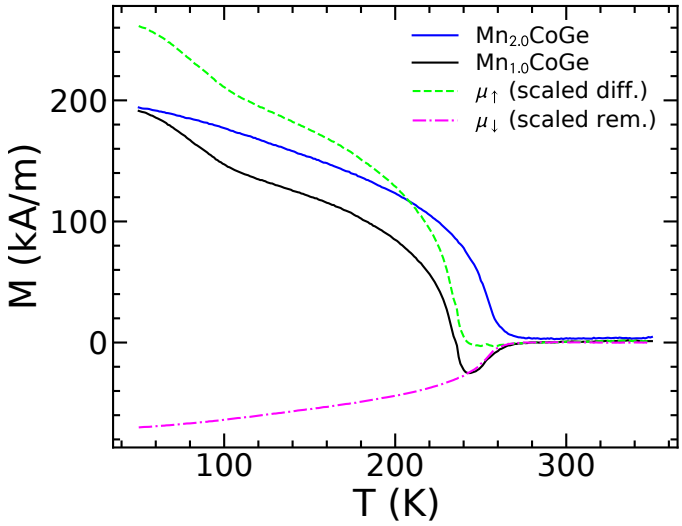

Figure 4.12: Hypothesis of two ferromagnetic domains that are antiferromagnetically coupled, where the moments are not equal in magnitude. The $Mn_{2.0}CoGe$ M_R (blue) curve is used as an estimate of the M_R of one magnetic sublattice (magenta) of the $Mn_{1.0}CoGe$ M_R curve (black), the difference yields the hypothetical M_R-T curve of the second sublattice (green).

Chapter 5

$Mn_\alpha RhGe$ alloys

This chapter presents the growth of $Mn_\alpha RhGe$ alloys. $Mn_{2.0}RhGe$ is predicted by DFT to form a tetragonal I$\bar{4}$2m structure, as does the related Mn_2RhSn Heusler. The Mn concentrations α were chosen to be the same as for the $Mn_\alpha CoGe$ samples. The $Mn_{2.0}RhGe$ system was of particular interest because it was hoped that it would behave similar to Mn_2RhSn (I$\bar{4}$2m). Another motivation to grow $Mn_\alpha RhGe$ was larger atomic number of Rh, when compared to Co, which leads to a larger spin-orbit interaction. MnCoGe has been heavily studied, while MnRhGe has hardly been studied at all and there are no reports of higher Mn content $Mn_\alpha RhGe$ [37, 69]. We therefore started with $Mn_{1.0}RhGe$ to enable comparison with bulk samples. Bulk MnRhGe is claimed to have a stable orthorhombic I$ma2$ (#46) TiFeSi-type-type structure [37], which is a deformation of a hexagonal P$\bar{6}$2m (#189) Fe_2P-type-structure. These are quite different from hexagonal $P6_3/mmc$ Ni_2In-type structure found in bulk $Mn_{1.0}CoGe$.

As in §4, GAXRD measurements are used to surpress the Si(004) peak to make crystallographic phase identification easier. The first thin-film $Mn_{1.0}RhGe$ samples were annealed at T=500 °C for 2 minutes, but XRD measurements only showed amorphous peaks. Increasing the annealing temperature up to 700 °C for 12 minutes yielded a P$\bar{6}$2m Fe_2P-type structure, as shown in Figure 5.1. This is unexpected given the I$ma2$ TiFeSi-type structure reported in bulk, although the I$ma2$ and P$\bar{6}$2m structures are closely related. A secondary RhGe Pnma phase is also present in the sample. Further annealing of the MnRhGe produces additional diffraction peaks due to unaccounted phases.

The $Mn_{1.5}RhGe$ sample annealed at 700 °C for 2 minutes was amorphous. The sample required annealing for a total of 47 minutes in order to crystallize (see Fig 5.2). As mentioned in §4, this sample did not experience an observable in-plane strain (see Fig 4.4), and revealed the same P$\bar{6}$2m Fe_2P-type structure, but without the secondary

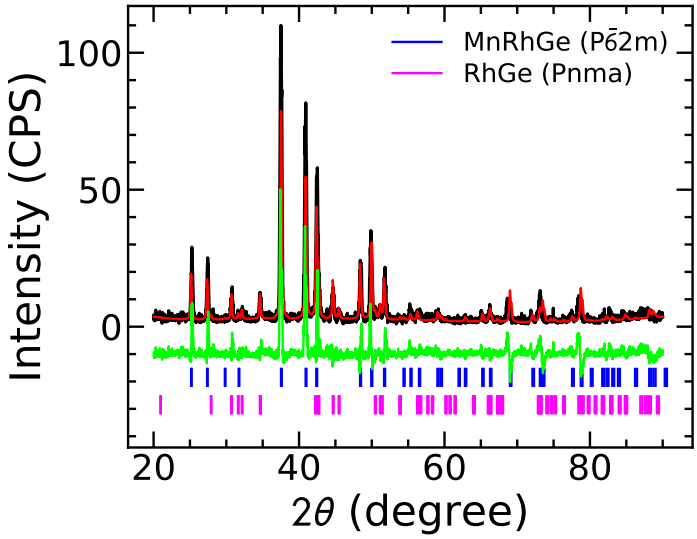

Figure 5.1: GAXRD diffraction pattern for $Mn_{1.0}$RhGe annealed at 700 °C for 12 minutes, with two distinct phases: MnRhGe P$\bar{6}$2m Fe_2P-type structure, and RhGe Pnma structure.

RhGe phase. The sample did delaminate after 47 minutes of annealing, but had large enough pieces remaining on the substrate to allow for GAXRD/XRD measurements. The peak intensities still showed evidence of a textured film.

$Mn_{2.0}$RhGe samples were annealed at 700 °C, initially for 2 minutes, which produced a P$6_3/mmc$ Ni_2In-type structure, as seen in the Mn_αCoGe samples (see Fig 4.7). $Mn_{2.0}$RhGe was further annealed for a total of 17 minutes. Figure 5.2c shows that this transformed the film to the orthorhombic I$ma2$ TiFeSi-type structure observed in bulk MnRhGe, which has 21 atoms within the TiFeSi-type I$ma2$ unit cell. A determination of the amount of vacancies on the 2a sites is not possible if Rh site disorder is also included. There was an attempt at fitting the P$\bar{6}$2m phase to the $Mn_{2.0}$RhGe sample, however, there were unaccounted peaks that could not be satisfied from possible RhGe phases. Figure 5.3 shows the (110) I$ma2$ diffraction peak of $Mn_{2.0}$RhGe, that is has an appropriate ratio when compared to the (011) I$ma2$ peak. The (110) peak is not present in the P$\bar{6}$2m $Mn_{1.0}$RhGe and $Mn_{1.5}$RhGe fits, and is not accounted for by the RhGe secondary phase.

The fact that the hexagonal P$6_3/mmc$ Ni_2In-type structure of $Mn_{2.0}$RhGe did not survive longer annealing times implies it is a metastable phase. Annealing at lower

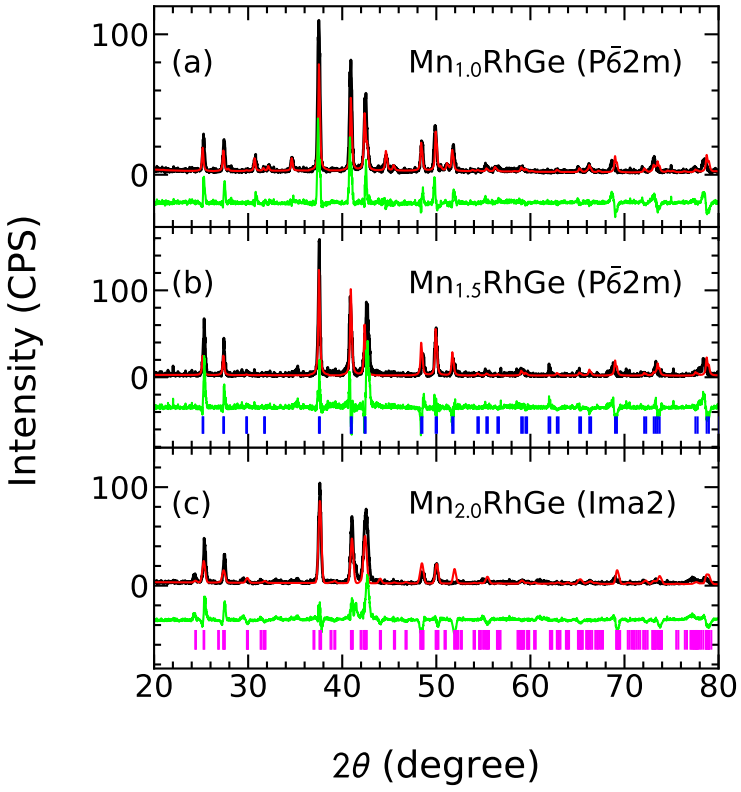

Figure 5.2: GAXRD patterns for $Mn_{1.0}RhGe$ (a), $Mn_{1.5}RhGe$ (b), and $Mn_{2.0}RhGe$ (c) found at annealing temperature of 700 °C. The P$\bar{6}$2m phase is found on $Mn_{1.0}RhGe$ and $Mn_{1.5}RhGe$ after annealing at 12 minutes and 47 minutes respectively. The Ima2 TiFeSi-type structure is found on $Mn_{2.0}RhGe$ after 17 minutes of annealing. The crystal peaks for P$\bar{6}$2m (blue), and Ima2 (magenta) are located below the residuals of the relevant fits.

temperatures also revealed a metastable phase in $Mn_{1.5}RhGe$. Figure 5.5a shows a $P6_3/mmc$ Ni_2In-type structure after annealing at 500 °C for 2 minutes. As no Ni_2In-type structure was found in $Mn_{1.0}RhGe$, the data suggest that excess Mn helps to form this metastable structure.

Figure 5.4 shows the evidence of a textured film for $Mn_{2.0}RhGe$ Ni_2In-type structure. XRD measurements show a much larger intensity for the 002, 102 and 2$\bar{1}$0 peaks compared to GAXRD. This discrepancy makes it difficult to achieve a reasonable refinement. Figure 5.7 shows evidence of (002) crystallites as hexagonal grains within the scanning electron microscopy image of $Mn_{2.0}RhGe$.

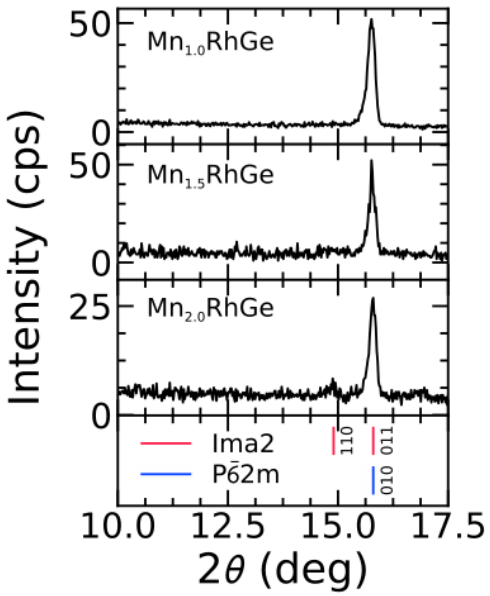

Figure 5.3: GAXRD of the $Mn_{\alpha}RhGe$ showing the difference between the Ima2 and P$\bar{6}$2m structures.

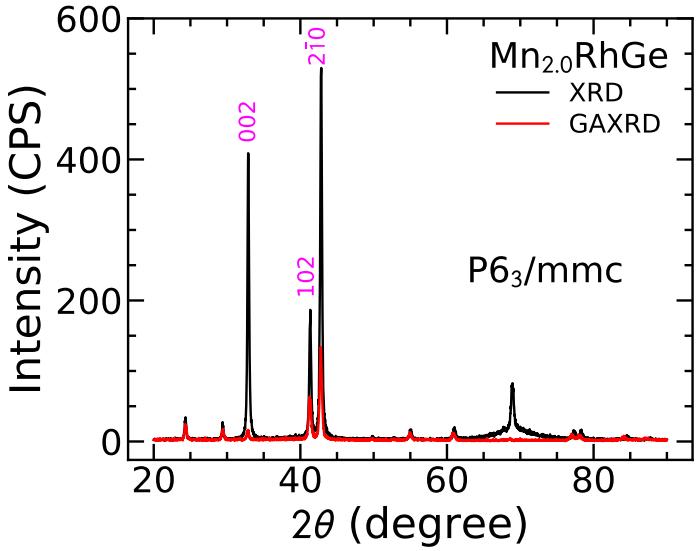

Figure 5.4: Discrepancy of 002, 102 and 2$\bar{1}$0 peaks for the $Mn_{2.0}RhGe$ Ni_2In-type structure in GAXRD, and XRD. The preferred orientations are possibly due to the surface energy differences from the $Mn_{\alpha}CoGe$ because Rh has a higher annealing temperature.

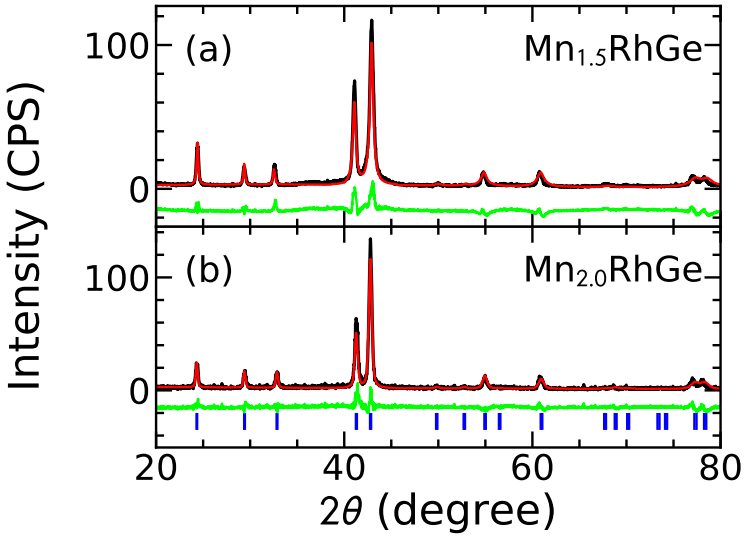

Figure 5.5: GAXRD patterns of $Mn_{1.5}RhGe$, and $Mn_{2.0}RhGe$ show $P6_3/mmc$ Ni_2In-type structures. Annealing of the Ni_2In-type structures found (a) $Mn_{1.5}RhGe$ at 700 °C, and (b) $Mn_{2.0}RhGe$ at 500 °C.

The $Mn_\alpha RhGe$ lattice parameters are tabulated in Table 5.3. To check whether the deposition process was preventing the Heusler alloy from forming, $Mn_{2.0}RhSn$ was sputter deposited. *Ex situ* annealing at 700 °C for 2 minutes yielded a tetragonal structure (see Fig 5.6), the lattice parameters a=430 pm and c=650 pm that were comparable to results found for bulk Mn_2RhSn [70].

Table 5.1: $Mn_\alpha RhGe$ parameters extracted from XRD, and comparisons.

Alloy	Phase	a (Å)	b (Å)	c (Å)	grain (nm)
$Mn_{1.0}RhGe$	$P\bar{6}2m$	6.51		3.53	45
$Mn_{1.5}RhGe$	$P6_3/mmc$	4.22		5.51	29
$Mn_{1.5}RhGe$	$P\bar{6}2m$	6.48		3.56	53
$Mn_{2.0}RhGe$	$P6_3/mmc$	4.23		5.45	52
$Mn_{2.0}RhGe$	$Ima2$	7.04	11.3	6.49	67
Mn_2RhSn (film/bulk)	$I\bar{4}m2$	4.30 / 4.29		6.50 / 6.62	
MnRhGe bulk	Hexagonal	6.545		3.570	
MnRhGe bulk	$Ima2$	7.12	11.34	6.56	

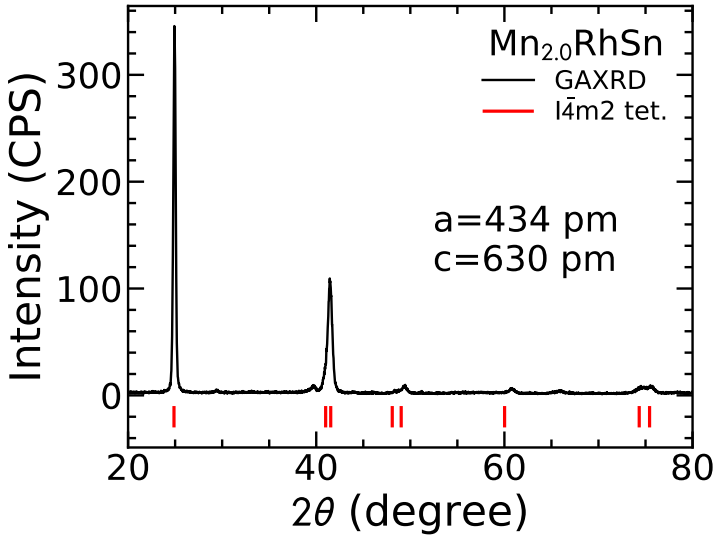

Figure 5.6: $Mn_{2.0}RhSn$ annealed at 700 °C for 2 minutes with preliminary results for the tetragonal $I\bar{4}m2$ structure (red). It is likely that material has a secondary phase for the unaccounted peaks.

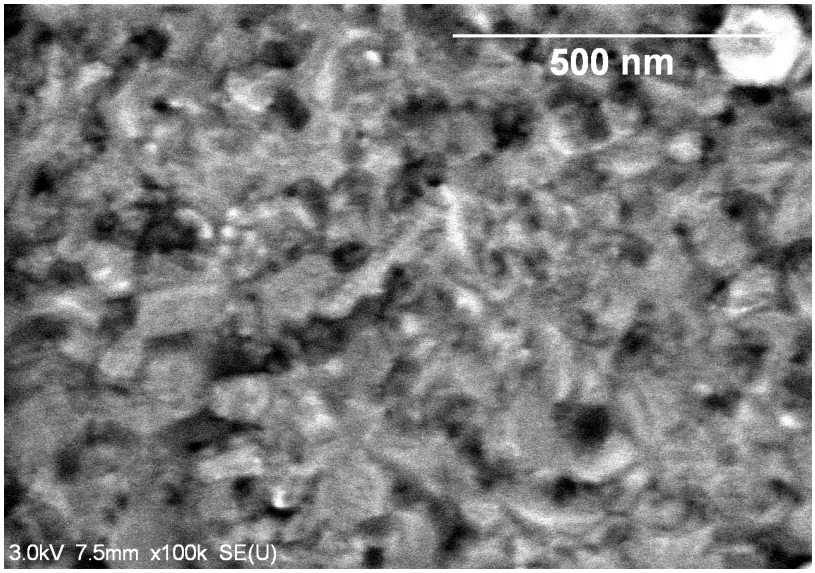

Figure 5.7: Scanning electron microscopy images showing evidence of grains on the order of 70 nm, found in $Mn_{2.0}RhGe$ of Ni_2In-type.

5.1 Magnetic characterization

5.1.1 Ni_2In-type structures

$Mn_\alpha RhGe$ samples were cut into (5.6×5.6) mm^2 $\pm$ 0.01 mm^2 squares, before two

to three pieces were loaded into the PPMS sample holder. Figure 5.8 shows the magnetic hysteresis curves for $Mn_{1.5}RhGe$, and $Mn_{2.0}RhGe$ for the Ni_2In-type structures, with the $M_{\rm sat}$=341.9 kA/m and 389.2 kA/m respectively (1.819 μ_B/f u and 2.34 μ_b/f u) comparable to the $Mn_{1.5}RhGe$ and $Mn_{2.0}RhGe$ samples. However, the magnetic hysteresis curves of the Ni_2In-type $Mn_\alpha RhGe$ show much larger coercive fields: $\mu_B H_C$=0.45 T for $Mn_{1.5}RhGe$ and 1.1 T for $Mn_{2.0}RhGe$.

The $Mn_{2.0}RhGe$ hysteresis shows an unusual step near $\mu_0 H_{ext} = 0$. This is likely due to a secondary phase with a much smaller coercive field. This soft magnetic phase can be separated from the $M - H$ loop by fitting it to a Langevin function

$$L(y) = \coth(y) - \frac{1}{y}, \tag{5.1}$$

where y is $\mu_m B/k_B T$.

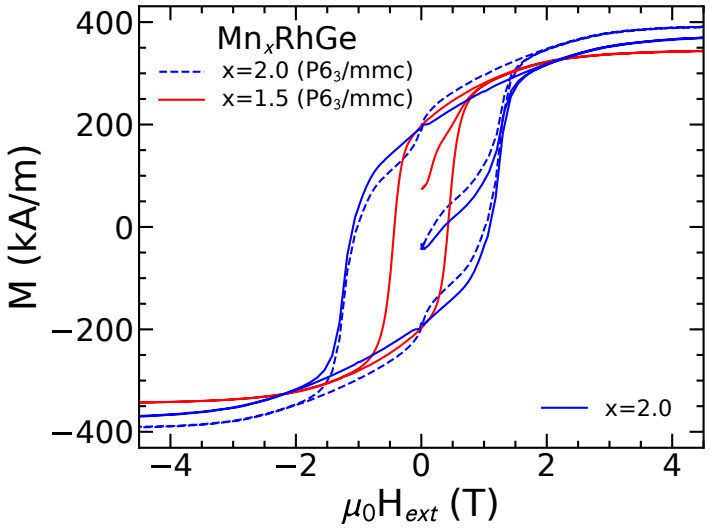

Figure 5.8: The magnetic hysteresis curves for $Mn_{1.5}RhGe$ (red) and $Mn_{2.0}RhGe$ (dotted blue) $P6_3/mmc$ Ni_2In-type structures, with $M_{\rm sat}$ values at 341.9 kA/m and 389.2 kA/m respectively. The solid blue curve shows $Mn_{2.0}RhGe$ after subtracting the soft magnetic phase.

The magnetization of the soft component represents 10% of the total M. Figure 5.9 shows the M_R-T of Ni_2In-type $Mn_{1.5}RhGe$, and $Mn_{2.0}RhGe$, without stripping off the soft magnetic impurity. The Curie temperature can be estimated to be 307 K for both samples. It is difficult to identify the crystallographic phase of the soft

magnetic impurity, as GAXRD measurements do not show any contributions from the other phases. The M_{sat} of the soft magnetic impurity is 37.2 kA/m at 5 K, and is still ferromagnetic at 350 K.

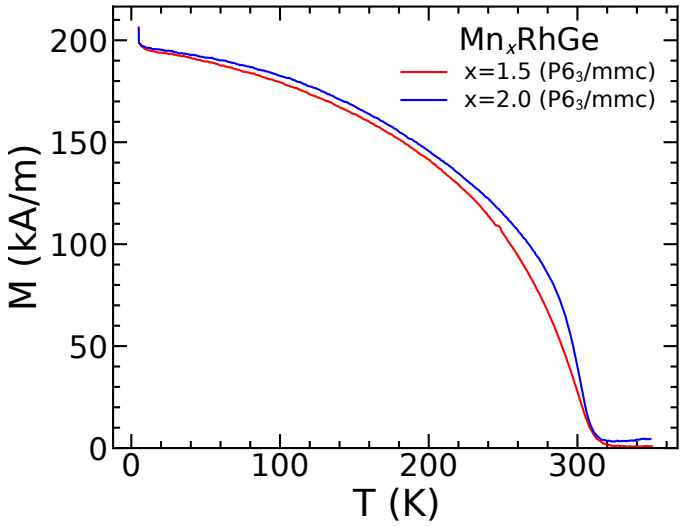

Figure 5.9: Remanent magnetization curves showing the T_C for $Mn_{1.5}RhGe$ (red), and $Mn_{2.0}RhGe$ (blue) Ni_2In-type structures. Curie Temperatures of $Mn_{1.5}RhGe$, and $Mn_{2.0}RhGe$ are estimated to be 307 K.

Unlike the Ni_2In-type $Mn_\alpha CoGe$, the $Mn_{2.0}RhGe$ Ni_2In-type hysteresis curve can be fit by the Stoner-Wohlfarth model outlined in §3.2.1. The model assumes each grain acts as a single domain uniaxial particle where the direction of the easy axis of the anisotropy is dermined by the random crystallographic orientation. Figure 5.10 compares the single domain model with the $Mn_{2.0}RhGe$, with the soft magnetic component removed. The good agreement between the model and measurements suggests that the magnetization reverses by coherent rotation of the magnetization within each grain. The small grain size, of the order of 70 nm, drives the system to a single domain state [3]. From Eq. (3.7) for the single domain model, the magnetocrystalline anisotropy is estimated to yield 0.417 MA^2/m^2. This value is comparable to other known K_u values for hard magnets such as Mn_3Ge, Mn_3Ga, and NbFeB in Table 5.2 [71, 72].

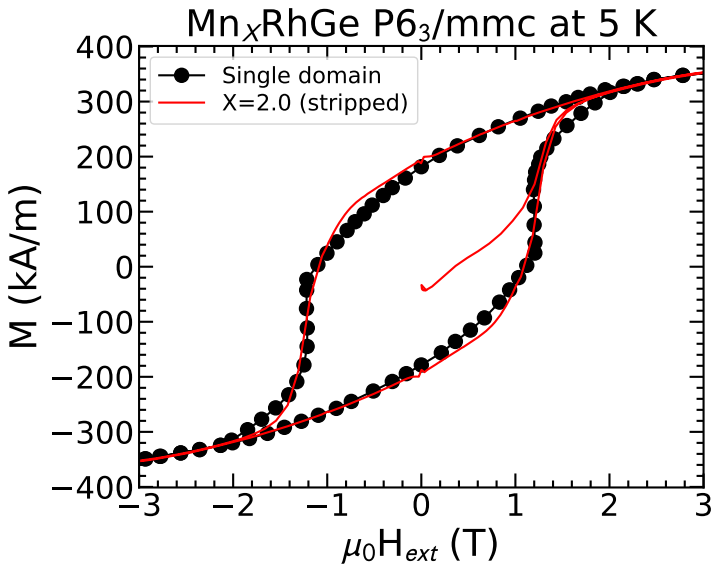

Figure 5.10: The Stoner-Wohlfarth model (red) overlayed on top of the $Mn_{2.0}RhGe$ magnetic hysteresis curve.

Table 5.2: Magnetocrystalline anisotropy comparison.

	$Mn_{2.0}RhGe$	Mn_3Ge	Mn_3Ga	NdFeB [73]
K_u (MJ/m^3)	0.411	1.0	0.91	4.9

5.1.2 Fe_2P-type, and TiFeSi-type structures

The higher temperature Fe_2P-type and TiFeSi-type structures have much smaller coercive fields than the Ni_2In-type. However, M_{sat} is significantly larger: M_{sat}=595.4 and 431.2 kA/m for $Mn_{1.0}RhGe$, and $Mn_{1.5}RhGe$ respectively (see Figure 5.11). The Curie temperature for bulk MnRhGe is T_C=420 K and is the only reliable magnetic property known [69].

The $Mn_{2.0}RhGe$ TiFeSi-type structure shows evidence of a secondary phase with a broadened coercive field near the M_{sat}, as shown by the step in the $M-H$ loop at $\mu_0 H_{ext}$=1.2 T. Unlike the Ni_2In-type $Mn_{2.0}RhGe$, the harder magnetic impurity cannot be easily subtracted.

The M_R-T for the $Mn_\alpha RhGe$ Fe_2P-type and TiFeSi-type structures show that the Curie temperature exceeds the 350 K limit of the PPMS (see Fig. 5.12). The $Mn_{1.0}RhGe$ and $Mn_{2.0}RhGe$ steps in the M_R-T curves above 290 K suggest a secondary magnetic phase. The $Mn_{1.5}RhGe$ P$\bar{6}$2m Fe_2P-type structure appears to be

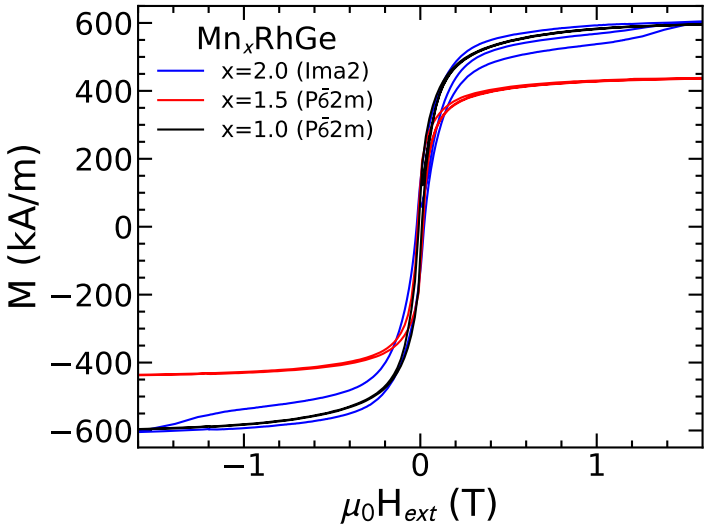

Figure 5.11: Magnetic hysteresis curves for P$\bar{6}$2m phases $Mn_{1.0}$RhGe (a) and $Mn_{1.5}$RhGe (b), with the Ima2 phase $Mn_{2.0}$RhGe (c). Hard magnetic impurity present on $Mn_{2.0}$RhGe (c), the opposite of the $Mn_{2.0}$RhGe Ni_2In-type phase (Fig 5.8).

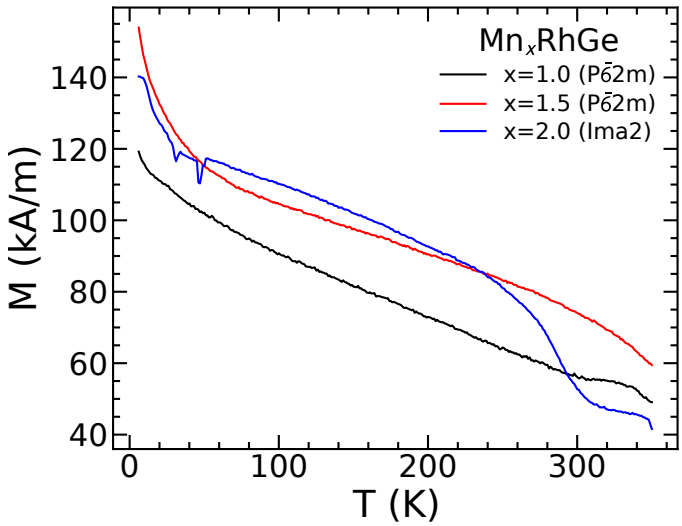

Figure 5.12: Remanent magnetization for the P$\bar{6}$2m, and Ima2 phases of the Mn, Rh, and Ge ternary alloys show that the Curie temperature is well above 350 K. Magnetic impurity phases can be seen in the Curie temperature curves, but this is due to annealing temperature, and duration choices.

more homogeneous based on the $M_R - T$ curvature. The $Mn_{2.0}$RhGe Ima2 sample slipped twice between 30-60 K, which can be seen as two transients the M_R-T curve.

Table 5.3: $Mn_{\alpha}RhGe$ magnetic characteristics and comparisons.

Alloy	Phase	M_{sat} (kA/m)	M_{sat} (μ_B/f.u.)	$\mu_0 H_C$ (T)	T_C (K)
$Mn_{1.0}RhGe$	P$\bar{6}$2m	605	2.82	0.0084	>350
$Mn_{1.5}RhGe$	P$6_3/mmc$	346	1.85	0.43	310
$Mn_{1.5}RhGe$	P$\bar{6}$2m	442	2.41	0.015	>350
$Mn_{2.0}RhGe$	P$6_3/mmc$	354	2.31	1.10	310
$Mn_{2.0}RhGe$	I$ma2$	622	1.65	0.021	>350
Mn_2RhSn (film/bulk)	I$\bar{4}$m2	305	1.97	0.065	∼280
MnRhGe bulk	Hexagonal				420
MnRhGe bulk	I$ma2$				

Kapton tape was affixed to the sample holder to prevent the samples from dropping in the chamber. Although for the measurements of $Mn_{2.0}RhGe$ it is likely that the samples slipped at these temperatures.

For the $Mn_{\alpha}RhGe$ films, there are a variety of crystallographic phases that were found: two hexagonal (P$6_3/mmc$, and P$\bar{6}$2m), and an orthorhombic phase (I$ma2$). None of the $Mn_{\alpha}RhGe$ films showed any evidence of a tetragonal structure, unlike $Mn_{2.0}RhSn$. However, the orthorhombic I$ma2$ structure has the right point group symmetry (C_{2v}) for hosting Néel skyrmions, with a T_C well above room temperature. The $Mn_{2.0}RhGe$ TiFeSi-type structure would make an interesting research opportunity for thin-film skyrmion research if a suitable lattice matched substrate is found.

Thin-film $Mn_{1.0}RhGe$ Fe_2P-type (P$\bar{6}$2m) was found to have the same lattice parameters as the unidentified hexagonal bulk MnRhGe in reference [69]. The Curie temperature thin-film $Mn_{1.0}RhGe$ was found to be T_C>350 K, be 420 K, consistent with the value in [69]. Given the subtle difference between P$\bar{6}$2m and I$ma2$ the MnRhGe structure may have been misidentified as orthorhombic. This chapter, however, demonstrates that an increase in Mn the content of MnRhGe helps to stabilize the I$ma2$ structure.

Chapter 6

$Mn_{\alpha}IrGe$ alloys

Little is known about the $Mn_{\alpha}IrGe$ family of compounds. Aside from DFT calculations that predict the existence of cubic, and tetragonal Mn_2IrGe Heusler [13], there have been no studies of $Mn_{\alpha}IrGe$ alloys. $Mn_{\alpha}IrGe$ alloys were magnetron sputtered in three stoichiometries, α={1.0, 1.5, 2.0}. Only one identifiable phase was found for α=2.0. Annealing $Mn_{2.0}IrGe$ at 500 °C for 15 minutes formed the $P6_3/mmc$ Ni_2In-type structure. Figure 6.1 shows the diffraction pattern for both GAXRD and XRD measurements, where the $\theta - 2\theta$ data depicts a much larger intensity than expected for the (002) peak. The data show that the film has a strong (002) texture. Preferred orientation was noticeable in the $Mn_{\alpha}RhGe$, but was even stronger in the $Mn_{2.0}IrGe$ films. The (002) peak intensity of the XRD data is clearly much longer in the GAXRD data. The remaining peak intensities could not be fit either. However, the peak positions allow for phase identification and measurements of the lattice parameters. The lattice parameters in Table 6.1 show a comparable unit cell size to Ni_2In-type $Mn_{2.0}RhGe$.

Table 6.1: $Mn_{2.0}IrGe$ Ni_2In-type parameters

Alloy	Phase	Time (min)	a Å	c Å
$Mn_{2.0}IrGe$	$P6_3/mmc$	15	4.23	5.650

Figure 6.2 shows the hysteresis curve for $Mn_{2.0}IrGe$ data. There is a magnetically soft secondary phase visible in the 5 K that is subtracted by fitting it to a Langevin function with an $M_{sat} = 3$ kA/m. The saturation magnetization of the primary phase of the $Mn_{2.0}IrGe$ film, $M_{sat} = 103$ kA/m is 3 times lower that either the $Mn_{\alpha}RhGe$ or $Mn_{\alpha}CoGe$ alloys. This may be due to site disorder on the Wyckoff 2a sites, where most of the magnetic order is expected to reside based on MnCoGe. However, the difficulty in fitting the X-ray data makes it impossible to address this question.

The shape of the hysteresis curve is qualitatively different from the the $Mn_{\alpha}RhGe$

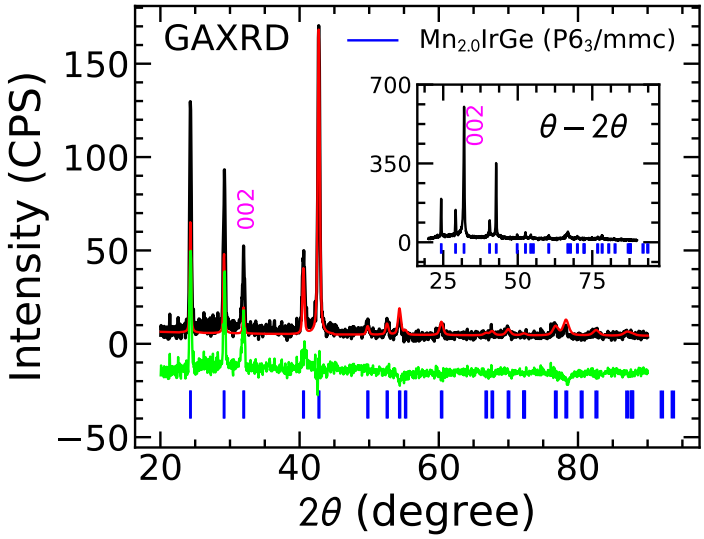

Figure 6.1: $Mn_{2.0}$IrGeGAXRD pattern displays the $P6_3/mmc$ Ni_2In-type structure, similar to $Mn_\alpha\{Co, Rh\}Ge$. The inset shows the $\theta - 2\theta$ XRD, with the 002 peak intensity dominating the diffraction pattern; the fit is shown in red, the residuals in green.

$P6_3$/mmc samples. The branch of the $M - H$ loop that starts from the demagnetized state, known as the virgin curve, has a small slope up to a field of $\mu_0 H_{ext}$=4 T, unlike the $Mn_{2.0}$RhGe samples. Here the magnetization reversal is dominated by domain wall motion, and this flat portion of the curve arises from domain wall pinning. The coercive field in this material, $\mu_0 H_C = 4.84$ T is huge, and points to a large magnetocrystalline anisotropy expected for Ir. The large anisotropy gives rise to smaller domain wall widths $\xi = \pi\sqrt{A/K_U}$ that would enable multi-domain states to form in the grains, where A is the exchange constant. These states lead to less skewed hysteresis loops, as compared to MnRhGe, that cannot be fit by a simple model in order to extract fundamental parameters of the film.

The hysteresis loop for $Mn_{2.0}$IrGe measured at $T = 300$ K shows no coercive field: the temperature is above T_C for the hard magnetic phase. However, the shape of the curve shows that the secondary soft magnetic phase is still ferromagnetic at room temperature. A coercive field of $\mu_0 H_C = 11$ mT is observed in this very soft phase with nearly zero M_R. However, the $M_R - T$ of the hard magnetic phase shows the characteristic drop in magnetization with increasing temperature, from which $T_C =$

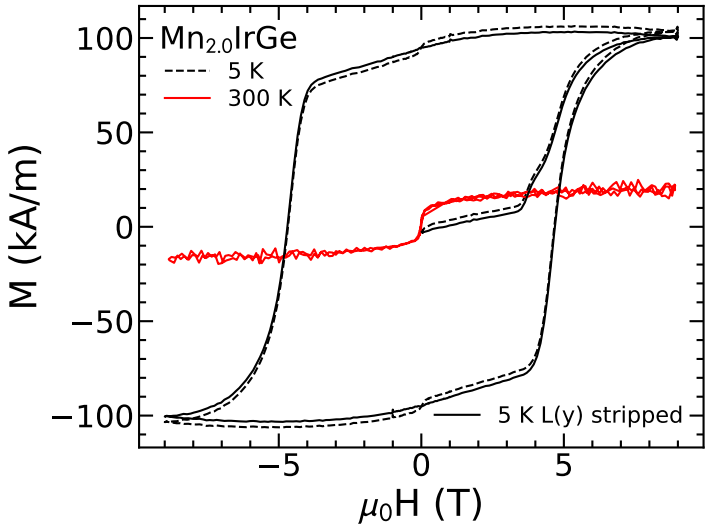

Figure 6.2: The 5 K magnetic hysteresis curve (dotted blue) for $Mn_{2.0}IrGe$ with a $\mu_0 H_C = 4.84$ T, and a $M_{\text{sat}} = 103.8$ kA/m. The 300 K magnetic hysteresis is shown to highlight a softer magnetic secondary phase with the $\mu_0 H_C = 0.011$ T, and M_{sat} 19 kA/m.

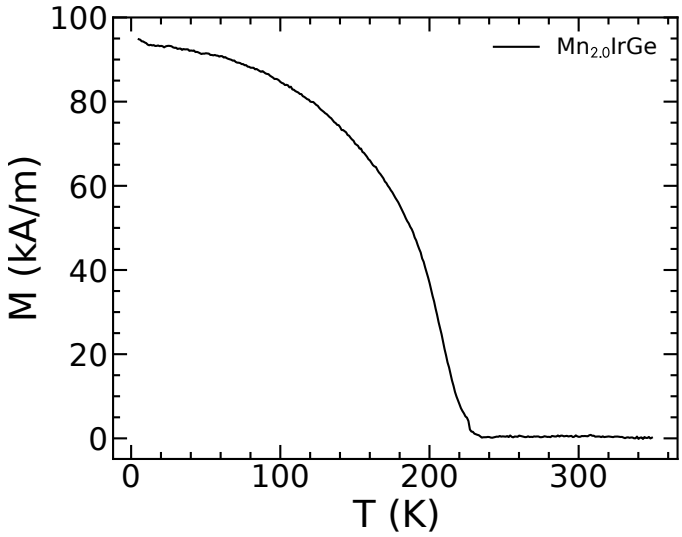

Figure 6.3: The $Mn_{2.0}IrGe$ T_C curve has similar characteristics to other $P6_3/mmc$ Ni_2In-type structures compared to the Co, and Rh variants. The Ni_2In-type $Mn_{2.0}IrGe$ has the lowest T_C of 224 K of all compounds presented in this research.

224 K is obtained for the primary phase (see Fig. 6.3.

Table 6.2: Summary of Ni_2In-type lattice parameters and magnetic characteristics.

Alloy	Anneal (°C)	M_{sat} (kA/m)	$M_{sat}(\mu_B$/f.u.)	$\mu_0 H_C$ (T)	T_C (K)
$Mn_{2.0}IrGe$	500	103	0.646	4.84	224

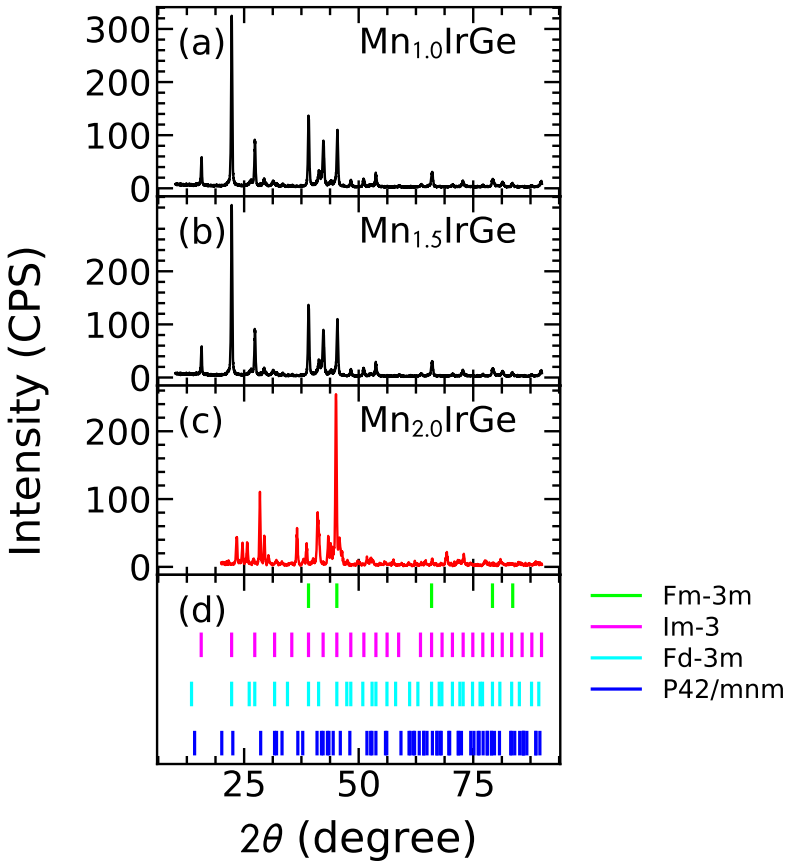

Figure 6.4: Diffractions patterns of $Mn_\alpha IrGe$ at 700 °C: (a) The $Mn_{1.0}IrGe$ annealed for 2 mintues, (b) $Mn_{1.5}IrGe$ annealed 22 minutes and (c) $Mn_{2.0}IrGe$ annealed for 2 minutes. Potential cubic and tetragonal phases for (a) and (b) can be seen in (d).

6.0.1 Future Work

As with previous $Mn_{1.0}CoGe$ and $Mn_{1.0}RhGe$ samples the $Mn_{1.0}IrGe$ sample was annealed multiple times at both 500 °C and 700 °C. An annealing temperature of 700 °C at 2 minutes show a diffraction pattern, that is different from the Ni_2In-type structure (see Fig 6.4a). A Rietveld refinement of the data was not successful. Secondary

phases and preferred orientation may be making the fitting difficult. Similarly fits were not successful for the other $Mn_{\alpha}IrGe$ alloys, α=1.0 and 1.5. The $Mn_{1.5}IrGe$ annealed at 700 °C for 22 minutes showed a similar diffraction pattern to $Mn_{1.0}IrGe$ (see Fig 6.4b). The structure of these alloys remains an open question for future work.

Chapter 7

Conclusion

This dissertation studied the family of thin-film compounds $Mn_{\alpha}CoGe$, $Mn_{\alpha}RhGe$ and $Mn_{\alpha}IrGe$ ($1 \leq \alpha \leq 2$) prepared by sputtering as potential candidates for inverse tetragonal full-Heuslers, based on DFT calculations [13]. Of the compounds studied, no inverse tetragonal structures were identified. However, two hexagonal Ni_2In-type ($P6_3/mmc$) and Fe_2P-type ($P\bar{6}2m$) materials were identified, in addition to an orthorhombic TiFeSi-type ($Ima2$) structure.

In the alloys studied, the Ni_2In-type ($P6_3/mmc$) was common to $Mn_{\alpha}CoGe$, $Mn_{1.5}RhGe$, $Mn_{2.0}RhGe$ and $Mn_{2.0}IrGe$ (see Fig 7.3,7.1). The Ni_2In-type structures in thin-films conforms to the results typical in high temperature MnCoGe bulk with defects. Defects in the film likely account for the reduction in M_{sat} compared to bulk crystals.

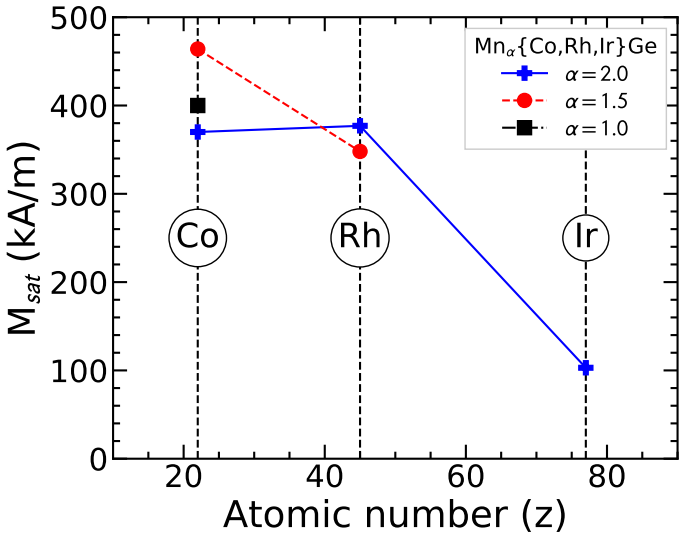

Figure 7.1: M_{sat} comparison of Ni_2In-type $Mn_{\alpha}\{Co, Rh, Ir\}Ge$ structures.

The Ni_2In-type structure discovered in $Mn_{1.5}RhGe$ an $Mn_{2.0}RhGe$ thin-films is a

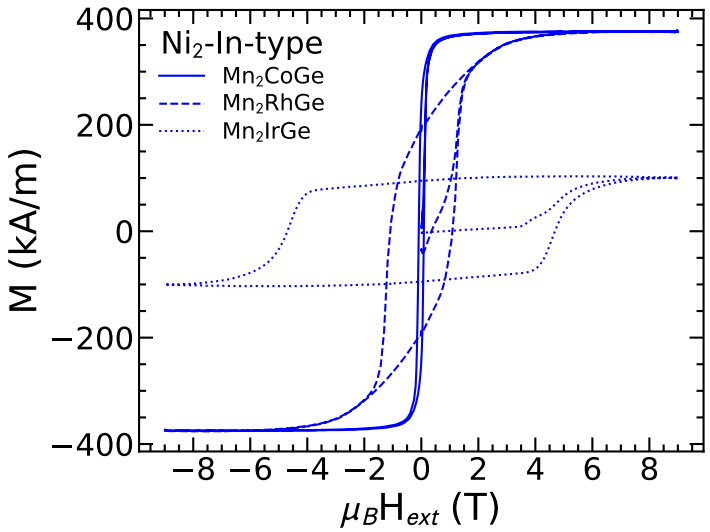

Figure 7.2: A comparison of the $M - H$ loops for $Mn_{2.0}CoGe$, $Mn_{2.0}RhGe$ and $Mn_{2.0}IrGe$ to emphasize how the hysteresis changes with increasing atomic number.

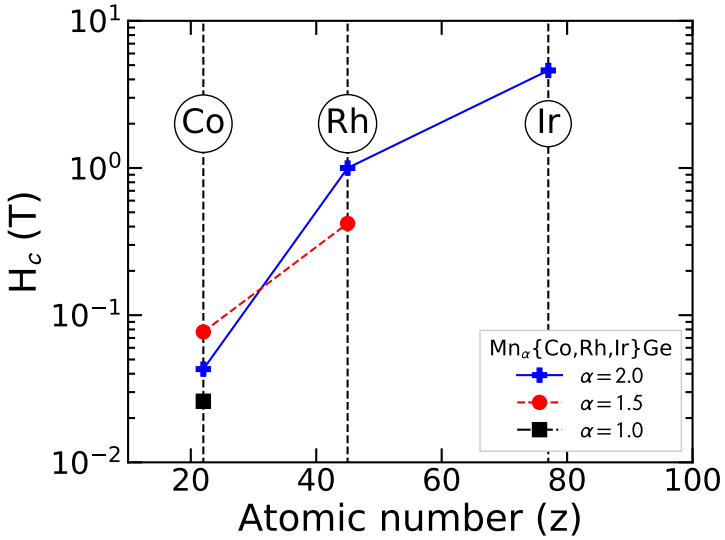

Figure 7.3: $mu_0 H_C$ comparison of Ni_2In-type $Mn_\alpha\{Co, Rh, Ir\}Ge$ structures.

new metastable phase not previously observed for these stoichiometries. The magnetization is comparable to the $Mn_\alpha CoGe$ alloys and suggests that the magnetic moment is due to Mn on the 2a sites, and is not significantly influenced by Co or Rh.

The larger atomic number for Rh does increase the spin-orbit interaction, which is demonstrated by the larger H_C. The Ni_2In-type $Mn_{2.0}RhGe$ $M-H$ loops that follow the Stoner-Wohlfarth model suggest the grains behave as single domain particles and allow for an estimate of the magnetocrystalline aniostropy.

The $Mn_{2.0}IrGe$ thin-film shows a Ni_2In-type metastable structure. However, film texturing poses difficulty in understanding the vacancies associated with the film. Figure 7.1 shows that the M_{sat} of $Mn_{2.0}IrGe$ is 1/3 the value of Co, and Rh Ni_2In-type alloys. Although Co and Rh don't appear to affect the 2a site in these alloys, it is not well understood how Ir affects the magnetization of the Ni_2In-type structure. This will need to be explored in future work. Figure 7.2 compares the $M-H$ loops for Ni_2In-type $Mn_{2.0}CoGe$, $Mn_{2.0}RhGe$ and $Mn_{2.0}IrGe$ materials.

The Fe_2P-type ($P\bar{6}2m$) structure was identified for $Mn_{1.0}RhGe$ and $Mn_{1.5}RhGe$ high temperature thin-films. The lattice parameters and T_C of the thin-films correspond to the unidentified hexagonal phase reported in bulk MnRhGe [69]. It is likely that MnRhGe bulk is a Fe_2P-type structure and the structure reported in [37] was misidentified as the TiFeSi-type ($Ima2$). What is not understood is how changing from Ni_2In-type to a Fe_2P-type structure causes the large drop in magnetocrystalline aniostropy.

During the writing of this thesis, it was discovered that magnetic screws were used on the sample table in the sputter system. These magnetic screws cause oscillatory behaviour in the material deposition (see Appendix B). To complete the analysis of the compounds studied here, samples will need to be regrown due to uncertainty in the deposition of the material. The figure shows that the sample thickness could vary by $\pm 20\%$ across the set of samples around the table in a given run. Fortunately the sample positions relative to the screws is fixed during the growth. If the magnetic field due to the screws affects each of the magnetrons by the same amount, the relative flux will not be affected. However, the powers for each of the magnetrons was different. Therefore the screws could have affected the stoichiometry of the films. However, the relative variation in the fluxes would be presumably significantly less than the 20% variation in absolute flux. Furthermore, this does not exceed the variation in the Mn composition in the grown alloys and the results of this work are relatively insensitive to Mn composition. Therefore, the results regarding the influence of alloy

composition on the crystal structure in this dissertation are suspected to be valid. However, the uncertainties in the film thickness deposited around the sputter table do increase the uncertainties in the value of the magnetization.

Bibliography

[1] Stuart S. P. Parkin, Masamitsu Hayashi, and Luc Thomas. Magnetic domain-wall racetrack memory. *Science*, 320(5873):190–194, 2008.

[2] Tanja Graf, Claudia Felser, and Stuart S.P. Parkin. Simple rules for the understanding of Heusler compounds. *Progress in Solid State Chemistry*, 39(1):1–50, 2011.

[3] S. Chikazumi and C.D. Graham. *Physics of Ferromagnetism 2e*. International Series of Monogr. OUP Oxford, 2009.

[4] S. Parkin, Xin Jiang, C. Kaiser, A. Panchula, K. Roche, and M. Samant. Magnetically engineered spintronic sensors and memory. *Proceedings of the IEEE*, 91(5):661–680, May 2003.

[5] I. Dzyaloshinsky. A thermodynamic theory of weak ferromagnetism of antiferromagnetics. *Journal of Physics and Chemistry of Solids*, 4(4):241 – 255, 1958.

[6] Murray Wilson, A.B. Butenko, A Bogdanov, and Theodore Monchesky. Chiral skyrmions in cubic helimagnet films: The role of uniaxial anisotropy. *Physical review. B, Condensed matter*, 89:094411, 03 2014.

[7] Theodore L. Monchesky. Detection with unpolarized currents. *Nature Nanotechnology*, 10:1008 EP –, Oct 2015.

[8] Niklas Romming, Christian Hanneken, Matthias Menzel, Jessica E. Bickel, Boris Wolter, Kirsten von Bergmann, André Kubetzka, and Roland Wiesendanger. Writing and deleting single magnetic skyrmions. *Science*, 341(6146):636–639, 2013.

[9] H. Wilhelm, M. Baenitz, M. Schmidt, U. K. Rößler, A. A. Leonov, and A. N. Bogdanov. Precursor phenomena at the magnetic ordering of the cubic helimagnet fege. *Phys. Rev. Lett.*, 107:127203, Sep 2011.

[10] H Wilhelm, M Baenitz, M Schmidt, C Naylor, R Lortz, U K Rler, A A Leonov, and A N Bogdanov. Confinement of chiral magnetic modulations in the precursor region of fege. *Journal of Physics: Condensed Matter*, 24(29):294204, 2012.

[11] Y Ishikawa, G Shirane, J A. Tarvin, and M Kohgi. Magnetic excitations in the weak itinerant ferromagnet mnsi. *Phys. Rev. B*, 16, 12 1977.

[12] G. Shirane. Magnetism of mnsi and fesi. In Umberto Balucani, Stephen W. Lovesey, Mario G. Rasetti, and Valerio Tognetti, editors, *Magnetic Excitations and Fluctuations II*, pages 157–161, Berlin, Heidelberg, 1987. Springer Berlin Heidelberg.

[13] Sergey V. Faleev, Yari Ferrante, Jaewoo Jeong, Mahesh G. Samant, Barbara Jones, and Stuart S.P. Parkin. Origin of the Tetragonal Ground State of Heusler Compounds. *Physical Review Applied*, 7(3):1–12, 2017.

[14] T Graf, S S P Parkin, and C Felser. Heusler compounds: A material class with exceptional properties. *IEEE Transactions on Magnetics*, 47(2):367–373, 2011.

[15] C. Felser, L. Wollmann, S. Chadov, G. H. Fecher, and S. S.P. Parkin. Basics and prospectives of magnetic Heusler compounds. *Springer Series in Materials Science*, 222(2015):37–48, 2016.

[16] C. Felser, L. Wollmann, S. Chadov, G. H. Fecher, and S. S.P. Parkin. Basics and prospectives of magnetic Heusler compounds. *Springer Series in Materials Science*, 222(2015):37–48, 2016.

[17] Ajaya K. Nayak, Vivek Kumar, Peter Werner, Eckhard Pippel, Roshnee Sahoo, Francoise Damay, Ulrich K. Rler, Claudia Felser, and Stuart Parkin. Discovery of magnetic antiskyrmions beyond room temperature in tetragonal heusler materials. *Nature*, 548, 03 2017.

[18] F Heusler. *Verh. Deutsche Physikalische Gesellschaft*, 5:219, 1903.

[19] S. Sakurada and N. Shutoh. Effect of Ti substitution on the thermoelectric properties of (Zr,Hf)NiSn half-Heusler compounds. *Applied Physics Letters*, 86(8):082105, 2005.

[20] Anindya Roy, Joseph Bennett, Karin Rabe, and David Vanderbilt. Half-Heusler Semiconductors as Piezoelectrics. *Physical review letters*, 109:037602, 07 2012.

[21] H. Mehnane, B. Bekkouche, S. Kacimi, A. Hallouche, M. Djermouni, and A. Zaoui. First-principles study of new half heusler for optoelectronic applications. *Superlattices and Microstructures*, 51(6):772 – 784, 2012.

[22] PJ Webster and KRA Ziebeck. Alloys and compounds of d-elements with main group elements. *Part*, 2:75–184, 1988.

[23] J. C. Slater. Atomic shielding constants. *Phys. Rev.*, 36:57–64, Jul 1930.

[24] S Skaftouros, Kemal zdoan, Ersoy Sasioglu, and I Galanakis. Generalized slater-pauling rule for the inverse heusler compounds. *Physical Review B*, 87, 10 2012.

[25] Margareta Elding-Pontn, Lars Stenberg, Ann-Kristin Larsson, Sven Lidin, and Kenny Sthl. Three $NiAsNi_2In$ Type Structures in the MnSn System. *Journal of Solid State Chemistry*, 129(2):231 – 241, 1997.

[26] C. Biswas, S. Banik, A. K. Shukla, R. S. Dhaka, V. Ganesan, and S. R. Barman. Surface composition and electronic structure of $Ni_{2+x}Mn_{1-x}Ga$ studied by X-ray photoelectron spectroscopy. *Surface Science*, 600(18):3749–3752, 2006.

[27] R. Fuglsby, P. Kharel, W. Zhang, S. Valloppilly, Y. Huh, and D. J. Sellmyer. Magnetism of hexagonal Mn(1.5)X(0.5)Sn (X = Cr, Mn, Fe, Co) nanomaterials. *Journal of Applied Physics*, 117(17):0–4, 2015.

[28] Wenhong Wang, Ying Zhang, Guizhou Xu, Licong Peng, Bei Ding, Yue Wang, Zhipeng Hou, Xiaoming Zhang, Xiyang Li, Enke Liu, Shouguo Wang, Jianwang Cai, Fangwei Wang, Jianqi Li, Fengxia Hu, Guangheng Wu, Baogen Shen, and Xi-Xiang Zhang. A centrosymmetric hexagonal magnet with superstable biskyrmion magnetic nanodomains in a wide temperature range of 100-340 k. *Advanced Materials*, 28(32):6887–6893, 2016.

[29] V. Franco, J. S. Blázquez, J. J. Ipus, J. Y. Law, L. M. Moreno-Ramírez, and A. Conde. Magnetocaloric effect: From materials research to refrigeration devices. *Progress in Materials Science*, 93:112–232, 2018.

[30] W. F. Giauque. A thermodynamic treatment of certain magnetic effects. a proposed method of producing temperatures considerably below 1 absolute. *Journal of the American Chemical Society*, 49(8):1864–1870, 1927.

[31] P. Debye. Einige bemerkungen zur magnetisierung bei tiefer temperatur. *Annalen der Physik*, 386(25):1154–1160, 1926.

[32] Ekkes Brück. Developments in magnetocaloric refrigeration. *Journal of Physics D: Applied Physics*, 38(23):R381, 2005.

[33] Yi Kun Fang, Jia Chun Yeh, Wen Cheng Chang, Xiu Mei Li, and Wei Li. Structures, magnetic properties, and magnetocaloric effect in MnCo(1-x)Ge (0.02<x<0.2) compound. *Journal of Magnetism and Magnetic Materials*, 321(19):3053–3056, 2009.

[34] J. B.A. Hamer, R. Daou, S. Özcan, N. D. Mathur, D. J. Fray, and K. G. Sandeman. Phase diagram and magnetocaloric effect of $CoMnGe_{1-x}Sn_x$ alloys. *Journal of Magnetism and Magnetic Materials*, 321(21):3535–3540, 2009.

[35] N. T. Trung, Z. Q. Ou, T. J. Gortenmulder, O. Tegus, K. H. J. Buschow, and E. Brck. Tunable thermal hysteresis in MnFe(P,Ge) compounds. *Applied Physics Letters*, 94(10):102513, 2009.

[36] B. Wurentuya, H. Yibole, F. Guillou, Zhiqiang Ou, Zhidong Zhang, and O. Tegus. First-order magnetic transition, magnetocaloric effect and moment formation in mnfe(p,ge) magnetocaloric materials revisited by x-ray magnetic circular dichroism. *Physica B: Condensed Matter*, 544:66 – 72, 2018.

[37] G. Venturini, B. Malaman, J. Steinmetz, A. Courtois, and B. Roques. Distribution des atomes metalliques dans les structures apparentees des trois composes ternaires equiatomiques : RhMnSi, isotype de Co2P, RhMnGe, isotype de TiFeSi et PdMnGe, isotype de Fe2P. *Materials Research Bulletin*, 17(2):259–267, 1982.

[38] M. F. Zumdick and R. Pttgen. Determination of the superstructures for the stannides zrirsn, hfcosn, and hfrhsn. *Zeitschrift f ur Kristallographie - Crystalline Materials*, 214(2):90–97, 2010.

[39] Donald M. Mattox. *Handbook of Physical Vapor Deposition (PVD) Processing (Second Edition)*. William Andrew Publishing, Boston, second edition edition, 2010.

[40] Kiyotaka Wasa, Isaku Kanno, and Hidetoshi Kotera. *Handbook of Sputter Deposition Technology: Fundamentals and Applications for Functional Thin Films, Nano-Materials and MEMS: Second Edition*. 2012.

[41] J. R. Dahn, S. Trussler, T. D. Hatchard, A. Bonakdarpour, J. R. Mueller-Neuhaus, K. C. Hewitt, and M. Fleischauer. Economical sputtering system to produce large-size composition-spread libraries having linear and orthogonal stoichiometry variations. *Chemistry of Materials*, 14(8):3519–3523, 2002.

[42] Lesker: Manganese (Mn) Sputtering Targets. "`https://www.lesker.com/newweb/deposition_materials/depositionmaterials_sputtertargets_1.cfm?pgid=mn1`". Accessed: 2017-11-15.

[43] SiO_2 Color Chart. "`http://fabweb.ece.illinois.edu/gt/gt/gt7.aspx`". University of Illinois, Department of Elecrical and Computer Engineering, Accessed: 2018-12-20.

[44] Y. Waseda, E. Matsubara, and K. Shinoda. *X-Ray Diffraction Crystallography: Introduction, Examples and Solved Problems*. Springer Berlin Heidelberg, 2011.

[45] R. Jenkins and R. Snyder. *Introduction to X-Ray Powder Diffractometry*. Chemical Analysis: A Series of Monographs on Analytical Chemistry and Its Applications. Wiley, 2012.

[46] N.W. Ashcroft and N.D. Mermin. *Solid State Physics*. HRW international editions. Holt, Rinehart and Winston, 1976.

[47] C. Kittel. *Introduction to Solid State Physics*. Wiley, 1996.

[48] S.H. Simon. *The Oxford Solid State Basics*. OUP Oxford, 2013.

[49] NIST: X-Ray Mass Attenuation Coefficients. "`https://www.nist.gov/pml/x-ray-mass-attenuation-coefficients`". Accessed: 2018-12-02.

[50] QuantumDesign. *Physical Property Measurement System*. 4 edition, 2003.

[51] Karhu Eric. *Structural and Magnetic Properties of Epitaxial MnSi(111) Thin Films*. PhD thesis, Dalhousie University, 2012.

[52] Yota Takamura, Akira Nishijima, Yohei Nagahama, Ryosho Nakane, and Satoshi Sugahara. Formation of Si- and Ge-based Full-Heusler Alloy Thin Films using SOI and GOI Substrates for the Half-metallic Source and Drain of Spin Transistors. *ECS Transactions*, 16(10):945–952, 2008.

[53] Yota Takamura, Takuya Sakurai, Ryosho Nakane, Yusuke Shuto, and Satoshi Sugahara. Epitaxial germanidation of full-Heusler Co2FeGe alloy thin films formed by rapid thermal annealing. *Journal of Applied Physics*, 109(7):109–112, 2011.

[54] J.F. Nye and P.P.L.J.F. Nye. *Physical Properties of Crystals: Their Representation by Tensors and Matrices*. Oxford science publications. Clarendon Press, 1985.

[55] L.D. Landau, E.M. Lifshitz, A.M. Kosevich, J.B. Sykes, L.P. Pitaevskii, and W.H. Reid. *Theory of Elasticity*. Course of theoretical physics. Elsevier Science, 1986.

[56] Sheng Can Ma, Dun Hui Wang, Hai Cheng Xuan, Ling Jia Shen, Qing Qi Cao, and You Wei Du. Effects of the Mn/Co ratio on the magnetic transition and magnetocaloric properties of $Mn_{1+x}Co_{1-x}Ge$ alloys. *Chinese Physics B*, 20(8):0–4, 2011.

[57] J.B.A. Hamer, R. Daou, S. Özcan, N.D. Mathur, D.J. Fray, and K.G. Sandeman. Phase diagram and magnetocaloric effect of $CoMnGe_{1-x}Sn_x$ alloys. *Journal of Magnetism and Magnetic Materials*, 321(21):3535–3540, nov 2009.

[58] C.F. Sánchez-Valdés, J.L. Sánchez Llamazares, H. Flores-Zúñiga, D. Ríos-Jara, P. Alvarez-Alonso, and Pedro Gorria. Magnetocaloric effect in melt-spun MnCoGe ribbons. *Scripta Materialia*, 69(3):211 – 214, 2013.

[59] Danlu Zhang, Zhihua Nie, Zilong Wang, Lian Huang, Qinghua Zhang, and Yan Dong Wang. Giant magnetocaloric effect in MnCoGe with minimal Ga substitution. *Journal of Magnetism and Magnetic Materials*, 387:107–110, 2015.

[60] Qingyong Ren, Wayne D. Hutchison, Jianli Wang, Andrew J. Studer, and Stewart J. Campbell. Magnetic and Structural Transitions Tuned through Valence Electron Concentration in Magnetocaloric $Mn(Co_{1-x}Ni_x)Ge$. *Chemistry of Materials*, 30(4):1324–1334, 2018.

[61] K Koyama and T Goto. Observation of an itinerant metamagnetic transition in MnSi under high pressure. 62(2):986–991, 2000.

[62] Jian-Tao Wang, Ding-Sheng Wang, Changfeng Chen, O. Nashima, T. Kanomata, H. Mizuseki, and Y. Kawazoe. Vacancy induced structural and magnetic transition in MnCo1xGe. *Applied Physics Letters*, 89(26):262504, dec 2006.

[63] S. Kaprzyk and S. Niziol. The electronic structure of CoMnGe with the hexagonal and orthorhombic crystal structure. *Journal of Magnetism and Magnetic Materials*, 87(3):267–275, jul 1990.

[64] Konstanze R. Hahn, Elie Assaf, Alain Portavoce, Sylvain Bertaina, and Ahmed Charaï. Structural and Composition Effects on Electronic and Magnetic Properties in Thermoelectric $Mn_{1-x-y}Co_{1+x}Ge_{1+y}$ Materials. *The Journal of Physical Chemistry C*, 121(48):26575–26586, dec 2017.

[65] A. Portavoce, E. Assaf, C. Alvarez, M. Bertoglio, R. Clrac, K. Hoummada, C. Alfonso, A. Chara, O. Pilone, K. Hahn, V. Dolocan, and S. Bertaina. Ferromagnetic MnCoGe thin films produced via magnetron sputtering and non-diffusive reaction. *Applied Surface Science*, 437:336 – 346, 2018.

[66] Giulia Avvisati, Claudia Cardoso, Daniele Varsano, Andrea Ferretti, Pierluigi Gargiani, and Maria Grazia Betti. Ferromagnetic and antiferromagnetic coupling of spin molecular interfaces with high thermal stability. *Nano Letters*, 18(4):2268–2273, 2018. PMID: 29558616.

[67] J. Dresselhaus, D. Spanke, F. U. Hillebrecht, E. Kisker, G. van der Laan, J. B. Goedkoop, and N. B. Brookes. Antiferromagnetic coupling of Mn adsorbates to Fe(100). *Phys. Rev. B*, 56:5461–5467, Sep 1997.

[68] Hatchard Timothy D. *Combinatorial studies of silicon-based alloy negatives for lithium-ion batteries*. PhD thesis, Dalhousie University, 2014.

[69] Tom A. Bither. Magnetic alloys of manganese, germanium and either or both of palladium and rhodium, June 1965. US Patent US3279914A.

[70] Vajiheh Alijani, Olga Meshcheriakova, Juergen Winterlik, Guido Kreiner, Gerhard H. Fecher, and Claudia Felser. Increasing Curie temperature in tetragonal Mn_2RhSn Heusler compound through substitution of Rh by Co and Mn by Rh. *Journal of Applied Physics*, 113(6):063904, feb 2013.

[71] J M D Coey. New permanent magnets; manganese compounds. *Journal of Physics: Condensed Matter*, 26(6):064211, 2014.

[72] NdFeB magnets/neodymium iron boron magnets datasheet. "`https://www.eclipsemagnetics.com/media/wysiwyg/datasheets/magnet_materials_and_assemblies/ndfeb_neodymium_iron_boron-standard_ndfeb_range_datasheet_rev1.pdf`". Eclipse Magnetics, Accessed: 2018-12-02.

[73] C. H. de Groot and Kees de Kort. Magnetoelastic anisotropy in ndfeb permanent magnets. *Journal of Applied Physics*, 85(12):8312–8316, 1999.

Appendix A

Magnetron calibration curves

This section includes the DC magnetron calibration curves for Mn, Co, Ge, Rh and Ir. Material was sputter deposited onto 1 cm × 1 cm Si(001) substrates, within a 2 mTorr Ar environment. The mass was measured prior and post deposition with a Satorius SE2 microbalance to determine the deposited mass. The dotted lines represent a linear extrapolation of the fit, which is only used as an estimate outside the region of data points. The linear estimate is not reliable below 20 W, as the target deposition rate is not a linear in this regime [68].

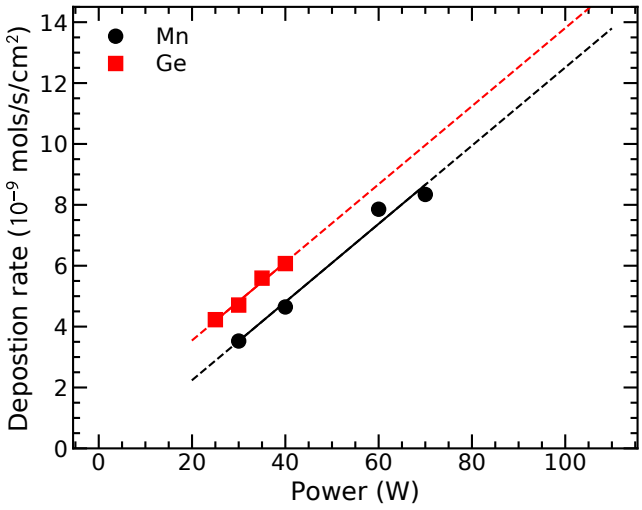

Figure A.1: Calibration for Mn and Ge targets in an 2 mTorr Ar environment

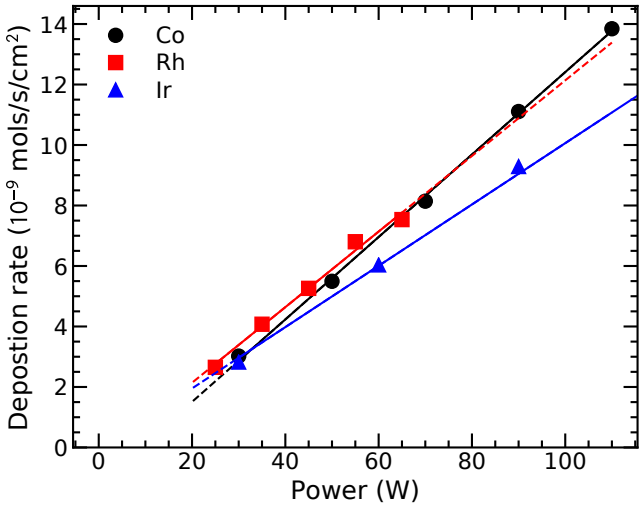

Figure A.2: Calibrations for Co, Rh and Ir targets in an 2 mTorr Ar environment

Appendix B

Stoichiometry uncertainty

During the writing of the dissertation Jason McCoombs tested the uniformity of the thickness of sputtered material around the table at the radial distance of 13.3 cm where samples were grown in this thesis. The deposition profile over the radius of 13.3 cm varies by 20% for deposition of Al at a power of 50 W. The oscillatory trend in the data correlates with the screw placements on the sputter table (see Fig B.2). The screws were magnetic and were found to affect the flux of the magnetron. Swapping the steel screws with brass screws resulted in a more uniform depositon profile.

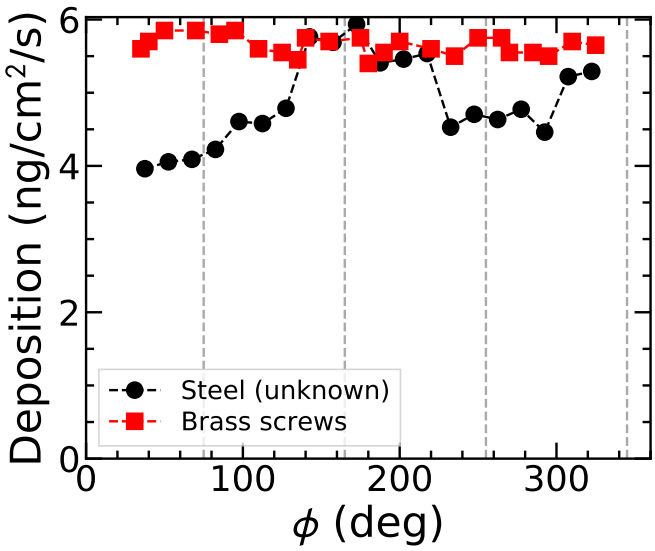

Figure B.1: Al sputter depositon profile that compares the presence of magnetic steel screws to brass screws on the sputter substrate table.

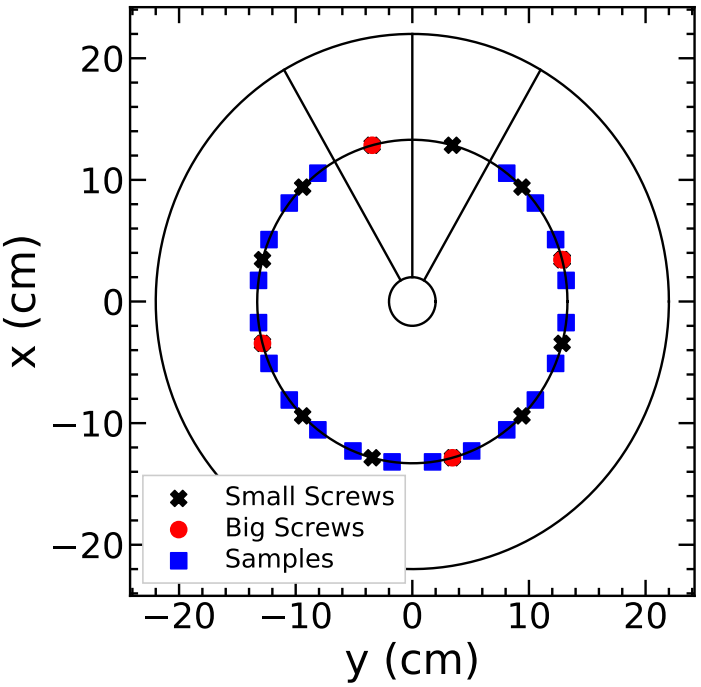

Figure B.2: Sputter substrate table layout for measuring the sputter deposition profile around the table at a radius 13.3 cm from the table centre. The dashed grey lines represent the placement of the big screws in Fig B.2.